

# Uranium metallogenesis of the peraluminous leucogranite from the Pontivy-Rostrenen magmatic complex (French Armorican Variscan belt): the result of long-term oxidized hydrothermal alteration during strike-slip deformation

C. Ballouard<sup>1,2</sup> · M. Poujol<sup>1</sup> · J. Mercadier<sup>3</sup> · E. Deloule<sup>4</sup> · P. Boulvais<sup>1</sup> · J. M. Baele<sup>5</sup> · M. Cuney<sup>3</sup> · M. Cathelineau<sup>3</sup>

Received: 30 November 2016 / Accepted: 13 August 2017 / Published online: 18 September 2017  
© Springer-Verlag GmbH Germany 2017

**Abstract** In the French Armorican Variscan belt, most of the economically significant hydrothermal U deposits are spatially associated with peraluminous leucogranites emplaced along the south Armorican shear zone (SASZ), a dextral lithospheric scale wrench fault that recorded ductile deformation from ca. 315 to 300 Ma. In the Pontivy-Rostrenen complex, a composite intrusion, the U mineralization is spatially associated with brittle structures related to deformation along the SASZ. In contrast to monzogranite and quartz monzodiorite ( $3 < U < 9$  ppm;  $Th/U > 3$ ), the leucogranite samples are characterized by highly variable U contents ( $\sim 3$  to 27 ppm) and Th/U ratios ( $\sim 0.1$  to 5) suggesting that the crystallization of magmatic uranium oxide in the more evolved facies was followed by uranium oxide leaching during hydrothermal alteration and/or surface weathering. U-Pb dating of uranium

oxides from the deposits reveals that they mostly formed between ca. 300 and 270 Ma. In monzogranite and quartz monzodiorite, apatite grains display magmatic textures and provide U-Pb ages of ca. 315 Ma reflecting the time of emplacement of the intrusions. In contrast, apatite grains from the leucogranite display textural, geochemical, and geochronological evidences for interaction with U-rich oxidized hydrothermal fluids contemporaneously with U mineralizing events. From 300 to 270 Ma, infiltration of surface-derived oxidized fluids leached magmatic uranium oxide from fertile leucogranite and formed U deposits. This phenomenon was sustained by brittle deformation and by the persistence of thermal anomalies associated with U-rich granitic bodies.

**Keywords** Uranium deposits · Syntectonic granites · Apatite geochemistry and U-Pb dating · Fluid-rock interactions · Hercynian · South Armorican shear zone

Editorial handling: R. L. Romer

**Electronic supplementary material** The online version of this article (<https://doi.org/10.1007/s00126-017-0761-5>) contains supplementary material, which is available to authorized users.

✉ C. Ballouard  
christopheballouard@hotmail.fr

<sup>1</sup> UMR CNRS 6118, Géosciences Rennes, OSUR, Université Rennes 1, 35042 Rennes Cedex, France

<sup>2</sup> Department of Geology, University of Johannesburg, PO Box 254, Auckland Park 2006, South Africa

<sup>3</sup> CNRS, CREGU, GeoRessources, Université de Lorraine, Boulevard des Aiguillettes, BP 70239, 54506 Vandoeuvre-lès-Nancy, France

<sup>4</sup> CRPG, UMR 7358 CNRS, Université de Lorraine, BP20, 54501 Vandoeuvre Cedex, France

<sup>5</sup> Department of Geology and Applied Geology, University of Mons, 20 Place du Parc, 7000 Mons, Belgium

## Introduction

Continental scale wrench faults represent common tectonic features in orogenic belts, which act as channels for crustal and mantle-derived magmas (Strong and Hanmer 1981; D'Lemos et al. 1992; Hutton and Reavy 1992; De Saint et al. 1998; Brown 2010; Pirajno 2010) as well as hydrothermal fluids (e.g., Sibson 1987, 1990; Faulkner et al. 2010; López-Moro et al. 2013; Cao and Neubauer 2016). Major strike-slip faults initiate deep within the crust and the lithospheric mantle due to rheological weakening (Cao and Neubauer 2016). During the exhumation of these tectonic systems, a thermal evolution occurs: brittle deformation (cataclases, pseudotachylytes) is superimposed on ductile deformation (mylonites) and the ascent of magmas as well

as hot lower crustal, and magmatic -derived fluids is followed by the downward flow of cold surface-derived water. Therefore, these strike-slip deformation zones can represent an important metallotect for hydrothermal uranium (U) deposits if they affect U fertile lithologies. Among U-rich igneous rocks, felsic volcanic rocks and peraluminous leucogranite represent an ideal source for the formation of hydrothermal U deposits because most of their U is hosted in easily leachable glass and uranium oxide, respectively (Cuney 2014). The relationships between U-rich felsic volcanic rocks, strike-slip faults, and hydrothermal uranium deposits are for example well illustrated in South China, along the southern termination of the Tan Lu fault (Li et al. 2001, 2002). Similarly, the association between peraluminous leucogranite, wrench faults, and U mineralization exists, for example, in Egypt along the El Sela shear zone (Gaafar et al. 2014; Gaafar 2015) and in the European Variscan belt (EVB): the Alentejo-Plasencia strike-slip fault in Iberia (Pérez Del Villar and Moro 1991) and the north-western part of the Massif Central (France; Cathelineau et al. 1990; Cuney et al. 1990; Gèbelin et al. 2009) (Fig. 1).

The Armorican Massif (France) in the EVB (Figs. 1 and 2) represents a historical mining province for U where about 20,000 t U (~20% of the French production; IRSN 2004) has been extracted before the end of the 1990s. Few minor deposits are associated with Late Carboniferous metaluminous granitoids emplaced along the north Armorican shear zone (NASZ; Chauris 1984), a crustal-scale, dextral, strike-slip fault with a limited displacement of ~20 km (Fig. 2) (Jégouzo 1980). The majority of the U deposits are spatially associated with Late Carboniferous peraluminous syntectonic leucogranite emplaced either along extensional deformation zones (Guérande leucogranite; Cathelineau 1981; Ballouard et al. 2017a) or along the south Armorican shear zone (SASZ: Mortagne and Pontivy leucogranites; Cathelineau 1982; Cathelineau et al. 1990; Cuney et al. 1990), a lithospheric-scale, dextral wrench fault with a displacement of ~200 km (Fig. 2) (Berthé et al. 1979; Gapais and Le Corre 1980; Jégouzo 1980; Jégouzo and Rossello 1988; Judenherc et al. 2003; Gumiaux et al. 2004a, b; Tartèse et al. 2012). Recent studies on mylonite, leucogranite, and quartz veins along the SASZ demonstrated that, during Late Variscan times, this fault acted as a major channel for lower crustal but also meteoric-derived oxidized hydrothermal fluids (Tartèse and Boulvais 2010; Tartèse et al. 2012; Lemarchand et al. 2012). These fluids were able to transport an important quantity of uranium in solution (Dubessy et al. 1987).

The Pontivy-Rostrenen syntectonic composite intrusion hosts U intragranitic deposits associated with peraluminous leucogranite (Figs. 2 and 3). U was interpreted to originate from leaching of uranium oxides from the surrounding leucogranite (Marcoux 1982), although the metallogenic model remains poorly constrained. In this study, we use

geochemical analyses and U-Pb dating of apatite from the granitoids as well as U-Pb dating of uranium oxides from the deposits to determine the timing and conditions of hydrothermal U mobilization and then its precipitation in the deposits. We then discuss this model in the geodynamic and metallogenic frameworks at the scale of the region and the EVB.

## Geological framework

### The Armorican Massif as part of the European Variscan belt

The Armorican Massif belongs to the EVB, a Paleozoic orogenic belt which extends throughout the western (Iberian Massif) and central Europe (Bohemian Massif) and results from the collision of supercontinents Laurussia and Gondwana (Ballèvre et al. 2009, 2013, 2014; Kroner and Romer 2013) (Fig. 1). The structure of the EVB is a consequence of a complex interaction between low-strain and high-strain domains (Kroner and Romer 2013). Low-strain domains, such as Ibero-Armorica, represent blocks of thick continental crust drifted from the northern Gondwana margin during Cambrian-Ordovician extension, whereas high-strain domains, such as the Massif Central and southern part of the Armorican Massif, that were highly deformed during Variscan orogeny, represent domains of Gondwana crust thinned during Lower Paleozoic extension (Kroner and Romer 2013). Continental subduction events in the Variscides occurred until ca. 350–340 Ma, and transition from a compressive to an extensive regime occurred ca. 315–300 Ma ago (Kroner and Romer 2013; Ballèvre et al. 2014).

The Armorican Massif is separated into three main domains by the NASZ and the SASZ (Fig. 2). The northern domain is mostly made of a Proterozoic basement (Brun et al. 2001), locally intruded by Variscan granitoids. The central domain is composed of Late Proterozoic (Brioverian) to Lower Carboniferous sedimentary rocks mostly deformed under greenschist facies conditions during dextral wrenching along the NASZ and SASZ in Carboniferous times (Gumiaux et al. 2004a). The deformation in this area is marked by a vertical foliation associated with a subhorizontal stretching lineation (Jégouzo 1980). The southern domain, which belongs to the internal part of the Variscan belt, is characterized by a higher degree of deformation and by the presence of high-grade metamorphic rocks (Gapais et al. 2015). Three tectono-metamorphic units can be distinguished in this domain and include, from top to bottom, HP-LT rocks, composed of blueschists and metavolcanic rocks subducted and exhumed during early tectonic events from 370 to 350 Ma (Bosse et al. 2005), micaschists, and migmatite-bearing units (Fig. 2). Between 315 and 300 Ma (Tartèse et al. 2012), the SASZ acted as a transfer zone between the southern domain,

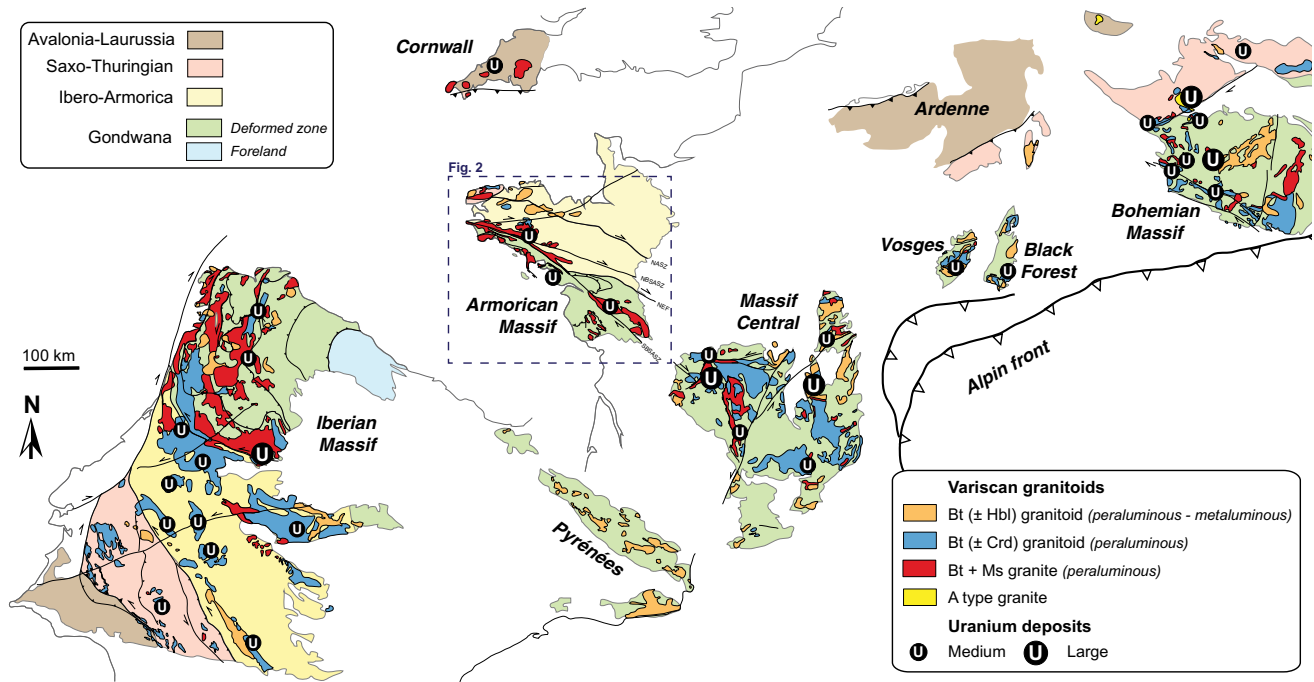


**Fig. 1** Schematic representation of the west European Variscan belt representing the main terranes (Ballèvre et al. 2009, 2013, 2016) and showing the relationship between Variscan granitoids and hydrothermal U deposits (after Cuney and Kyser 2008). The granite typology is based on the 1:1,000,000 geological maps of France (Chantraine et al. 2003), Portugal, and Spain (Civis Llovera 2015) and the 1: 500,000 geological

maps of Czechoslovakia (Fusán et al. 1967) and Czech Republic (Cháb et al. 2007). NASZ: north Armorican shear zone, NBSASZ: northern branch of the south Armorican shear zone, SBSASZ: southern branch of the south Armorican shear zone, NEF: Nort-sur-Erdre fault. Mineral abbreviations according to Whitney and Evans (2010)

where crustal extension led to the exhumation of core complexes cored by migmatites and synkinematic leucogranites, and the central domain deformed by pervasive dextral wrenching (Gapais et al. 2015).

During the Late Carboniferous, the Armorican Massif was intruded by various granitoids ranging from peraluminous to metaluminous in composition (Capdevila 2010; Fig. 2). To the south, two mica peraluminous leucogranites are characteristic. They were emplaced either along extensional deformation zone in the southern domain, such as the Quiberon (Gapais et al. 1993, 2015), Sarzeau (Turrillot et al. 2009), and Guérande ( $309.7 \pm 1.3$  Ma: Ballouard et al. 2015) leucogranites, or along the SASZ such as the Lizio ( $316.4 \pm 5.6$  Ma: Tartèse et al. 2011a), Questembert ( $316.1 \pm 2.9$  Ma: Tartèse et al. 2011b), and Pontivy ( $316.7 \pm 2.5$  Ma: Ballouard et al. 2017b) leucogranites. To the north, a bimodal magmatism occurred as expressed by the emplacement of biotite ± cordierite peraluminous granites, associated with intermediate rocks of mantle origin, such as the Rostrenen ( $315.5 \pm 2.0$  Ma: Ballouard et al. 2017b) and Huelgoat intrusions ( $314.8 \pm 2.0$  Ma: Ballouard 2016) and two suites of biotite ± hornblende metaluminous granitoids. These granitoids consist of a magneso-potassic and a ferro-potassic suite emplaced between 320 and 300 Ma and associated with mantle-derived mafic to intermediate rocks (Capdevila 2010; Ballouard et al. 2017b). On a regional scale, the crustal magmatism to the south of the SASZ

was triggered by late-orogenic crustal extension. In contrast, to the north, partial melting of the crust and mantle, enriched during earlier subduction events, was triggered by an asthenosphere upwelling during strike-slip deformation and subsequent slab-tearing (Ballouard et al. 2017b).

The EVB represents an important metallogenic province for U where vein, episyenite-type, breccia-hosted, or shear zone-hosted U deposits occur all over the belt. Major occurrences are located in the Iberian Massif, the Armorican Massif, the Massif Central, and the Bohemian Massif (Fig. 1). A large proportion of these hydrothermal U deposits are spatially associated with Late Carboniferous low Ca peraluminous two mica (or biotite) granite (Fig. 1) and main U mineralizing events in the EVB occurred during the Permian from 300 to 260 Ma (Cuney et al. 1990; Cathelineau et al. 1990; Tischendorf and Förster 1994; Cuney and Kyser 2008; Romer et al. 2010; Ballouard et al. 2017a).

In the Armorican Massif, U has been mostly mined in the Guérande, Pontivy, and Mortagne districts (Fig. 2). In the Guérande district, the most important vein deposit (Pen Ar Ran) is perigranitic and localized above the apical zone of the Guérande leucogranite (Cathelineau 1981). The Guérande leucogranite itself was the main source for U (Ballouard et al. 2017a). Trace elements and oxygen isotope compositions suggest that hydrothermal leaching of the magmatic uranium oxides in deformed facies of the apical zone

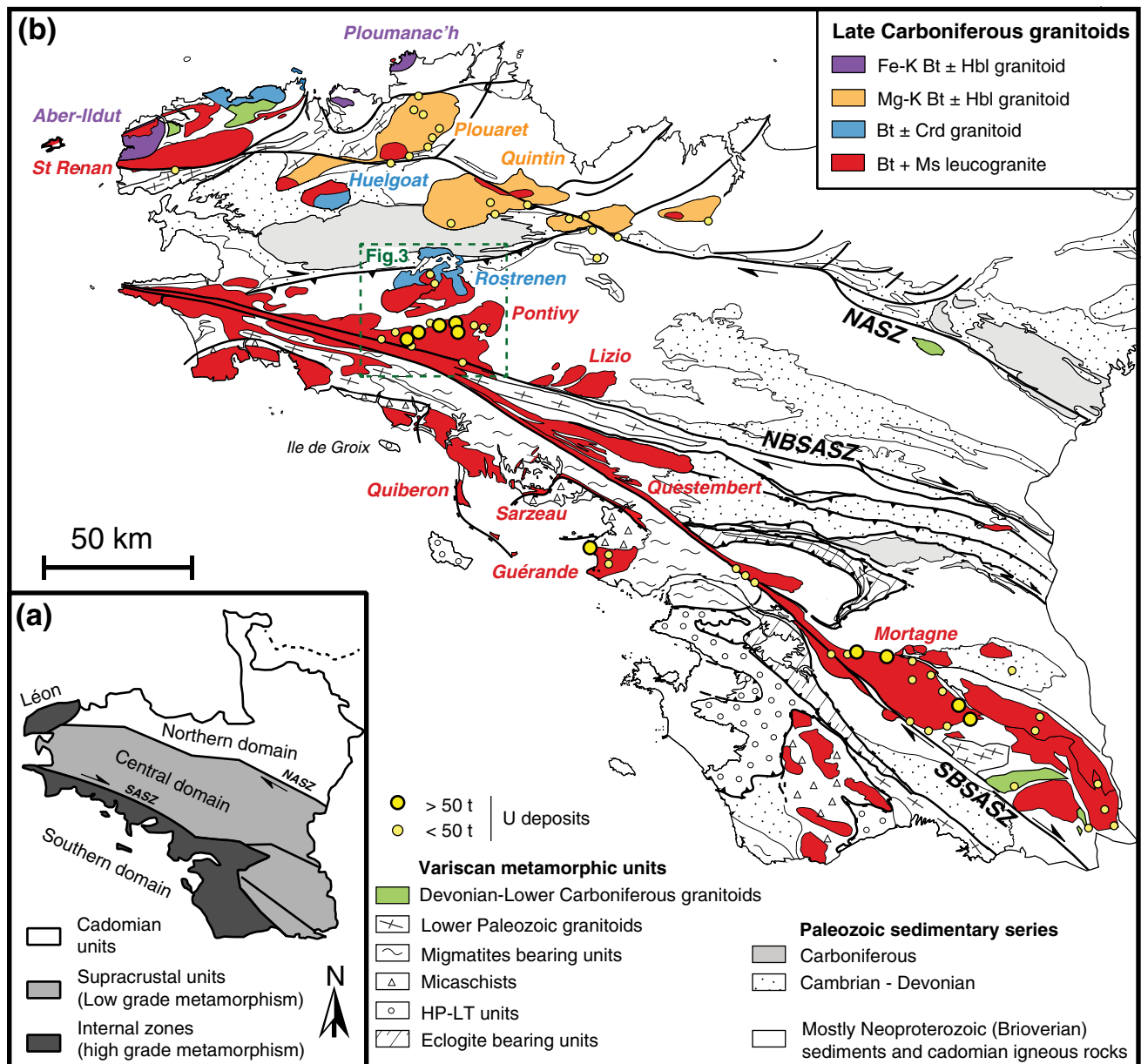


**Fig. 2** **a** Schematic structural map of the Armorican Massif. **b** General geological map of the Armorican Massif identifying the different types of Carboniferous granites, according to Capdevila (2010), and the locations of the principal U deposits. The geological map is modified from Chantraine et al. (2003), Gapais et al. (2015), and Ballouard et al.

(2017b). NASZ: north Armorican shear zone, SBSASZ: southern branch of the south Armorican shear zone, NBSASZ: northern branch of the south Armorican shear zone, Fe-K granitoid: ferro-potassic granitoid, Mg-K granitoid: magnesio-potassic granitoid. Mineral abbreviations according to Whitney and Evans (2010)

was promoted by the infiltration of surface-derived oxidized fluids. The leached U was then precipitated in the reducing environment represented by black shales and graphitic quartzites (Ballouard et al. 2017a). The age of the U mineralizing events in the Guérande area (ca. 300 to 275 Ma) is comparable with that in the Mortagne district and with other U deposits from the EVB (Cathelineau et al. 1990; Ballouard et al. 2017a). The Questembert leucogranite (Fig. 2) is not associated with U mineralization but the petrogeochemical and geochronological study of Tartèse et al. (2013) suggests that

this intrusion liberated an important amount of U during a subsolidus alteration event at depth, by surface-derived oxidized fluids.

### The Pontivy-Rostrenen magmatic complex

#### General framework

Gravimetric data reveals that the Pontivy-Rostrenen complex represents a continuous intrusion with the main root (~6 km

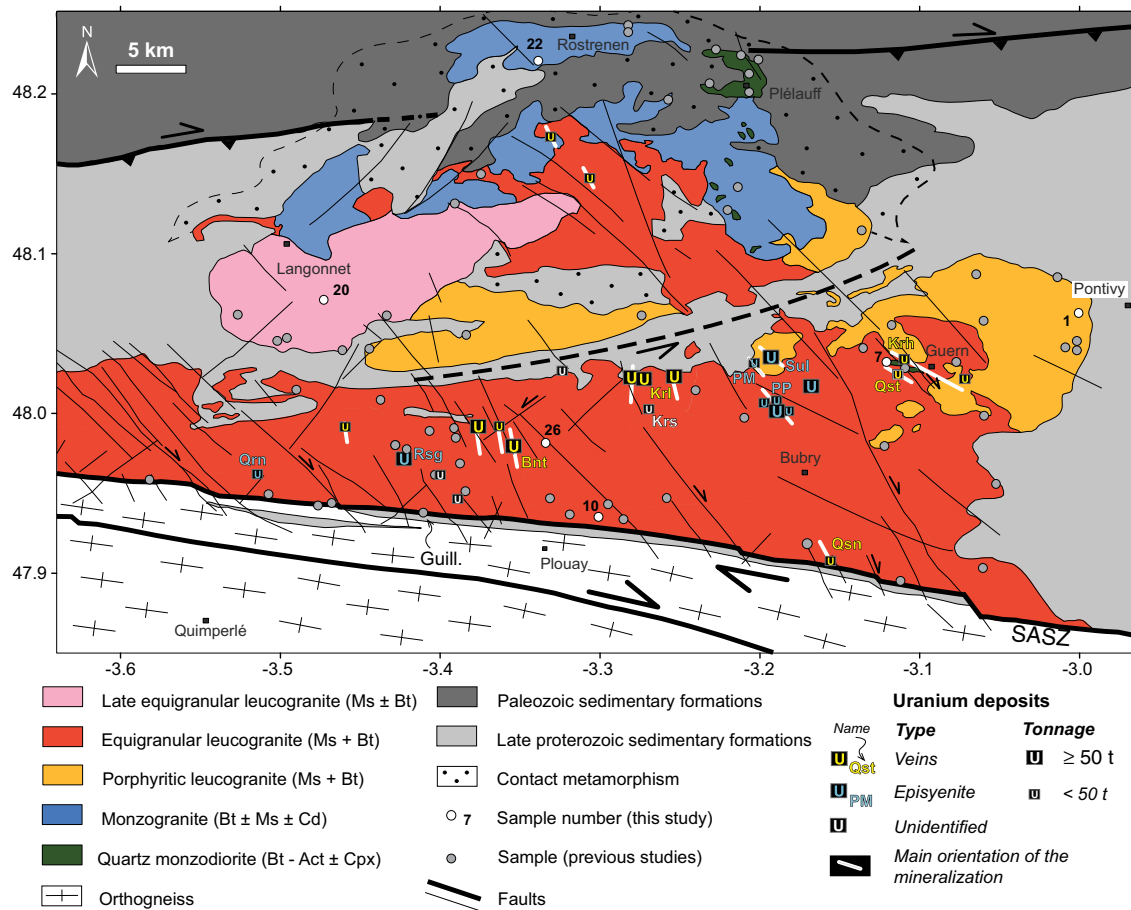


**Fig. 3** Geological map of the Pontivy-Rostrenen magmatic complex showing the different magmatic units and locations of U deposits. Sample locations from this and previous studies are shown on the map. The map is redrawn from Euzen (1993) and Ballouard et al. (2017b) and from the 1: 50,000 BRGM geological maps of Pontivy (Dadet et al. 1988), Rostrenen (Bos et al. 1997), Plouay (Béchenne et al. 2006), and

Bubry (Béchenne and Thiéblemont 2011). SASZ: south Armorican shear zone. The types of U deposits and their main orientations are from Marcoux (1982) and Cuney (2006). Qst: Quistiave, Krh: Kerroch, PM: Prat Mérien, PP: Poulprio, Sul: Sulliado, Qsn: Quistinic, Krl: Kerlech (Lignol), Bnt: Bonote, Rsg: Rosglas, Qrn: Quérien (Kerjean), Krs: Kerségalec, Guill.: Guilligomarch

depth) localized to the north (Vignerresse and Brun 1983; Vignerresse 1999). The southern part of the complex is composed almost exclusively of peraluminous leucogranite, whereas peraluminous leucogranite and monzogranite outcrop to the north with small stocks of mantle-derived metaluminous quartz monzodiorite (Fig. 3) (Euzen 1993; Ballouard et al. 2017b). To the south, leucogranite intrudes Late-Proterozoic (Brioverian) sedimentary rocks, whereas to the north, leucogranite, monzogranite, and quartz-monzodiorite intrude Late-Proterozoic and Paleozoic (Ordovician to Lower Carboniferous) sedimentary formations causing contact metamorphism (Fig. 3). Vignerresse (1999) estimated that these intrusions were emplaced at a depth around 6–8 km. The shape of the Pontivy leucogranite intrusion to the south marks the dextral shearing of the SASZ (Figs. 2 and 3), and in the southern edge, syn-cooling shearing is revealed by the development of C/S structures (Gapais 1989) and mylonites in 100 m wide dextral shear zones, oriented N100–110° (Jégouzo 1980). The oxygen isotope study carried

out on mylonites from the Guilligomarch quarry (Fig. 3) in the southern edge of the complex showed that some of these rocks experienced hydrothermal alteration by low δ<sup>18</sup>O meteoric-derived fluids (Tartèse et al. 2012).

*Petrogeochemical characteristics*

The petrogeochemistry and geochronology is summarized from Ballouard et al. (2017b). Leucogranite contains quartz-feldspar-muscovite with a variable amount of biotite that can be either absent or dominant over muscovite. Tourmaline is rarely observed. Common accessory minerals are zircon, apatite, monazite, and Fe-Ti oxides. Uranium oxides were not observed in our samples. This absence is likely the consequence of the instability of this mineral during postcrystallization alteration and/or weathering, because U oxides were commonly observed in the drill cores from leucogranite associated with U deposits, such as Guérande (Ouddou 1984) (Fig. 1), or in the northwestern part of the

Massif Central (Friedrich et al. 1987). The leucogranite was divided into three main subfacies (Fig. 3):

1. The porphyritic leucogranite is characterized by the abundance of K-feldspar megacrysts and a higher amount of biotite over muscovite.
2. The equigranular leucogranite represents the most common type of leucogranite in the complex and is characterized by a low abundance (or the absence) of K-feldspar megacrysts. The proportion of biotite over muscovite is variable, biotite being even absent in some cases.
3. The late equigranular leucogranite (Langonnet leucogranite) forms an elliptic stock which crosscuts the other facies. This leucogranite is rarely porphyritic and generally contains a low proportion of biotite.

In terms of alteration, chloritization of biotite is common and secondary muscovitization affects more particularly the muscovite > biotite equigranular facies. Several veins of pegmatite and aplite crosscut the leucogranite. Moreover, pegmatite stocks were described along the western edge of the late equigranular leucogranite and greisenization locally affects the most evolved parts of the equigranular and late equigranular leucogranites (Euzen 1993; Bos et al. 1997).

The monzogranite (Rostrenen granite) crops out in the northern part of the complex (Fig. 3). This facies contains a quartz-feldspar-biotite assemblage with a small amount of muscovite and, locally, cordierite. The most common accessory minerals include zircon, monazite, and Fe-Ti oxides. Mafic enclaves with a composition similar to quartz-monzodiorite are commonly observed in this facies (Euzen 1993). The quartz-monzodiorite facies mostly appears as small stocks of a few square kilometers in the eastern part of the monzogranitic intrusion (Fig. 3). This facies generally contains quartz-feldspar-biotite-amphibole  $\pm$  clinopyroxene as well as apatite, titanite, zircon, and Fe-Ti oxide as accessory minerals. Ocellar quartz is commonly observed in this facies and interpreted as the result of a mixing with a felsic magma. Mingling features are visible at the contact between the quartz-monzodiorite and the monzogranite.

U-Pb dating of magmatic zircon grains revealed that the three magmatic facies of the complex were emplaced synchronously between  $316.7 \pm 2.5$  and  $310.3 \pm 4.7$  Ma, whereas the late equigranular leucogranite was emplaced later at  $304.7 \pm 2.7$  Ma. The peraluminous leucogranite ( $A/CNK > 1.1$ ) has mostly subchondritic  $\varepsilon Nd(t)$  values ( $-4.79$  to  $+2.08$ ) and contains numerous inherited zircon grains with Archean to Paleozoic ages. It formed by partial melting of Neoproterozoic metasedimentary rocks and Paleozoic peraluminous orthogneisses. The moderately peraluminous monzogranite ( $1.0 < A/CNK < 1.3$ ) has a subchondritic  $\varepsilon Nd(t)$  composition ( $-3.95$  to  $-3.22$ ) and contains magmatic zircon with subchondritic  $\varepsilon Hf(t)$  values and scarce Paleozoic

inherited zircon. It formed by partial melting of an orthogneiss with a probable metaluminous composition. The metaluminous quartz monzodiorite ( $0.7 < A/CNK < 1.1$ ) has subchondritic  $\varepsilon Nd(t)$  values ( $-3.19$  to  $-2.17$ ) and contains magmatic zircon grains with sub- to slightly superchondritic  $\varepsilon Hf(t)$  values. It formed by partial melting of a metasomatized lithospheric mantle.

The evolution from high ( $\sim 70$  wt%) to very high ( $\sim 75$  wt%)  $SiO_2$  leucogranite is likely explained by the fractional crystallization of a cumulate composed of Bt + Kfs + Pl as well as accessory minerals such as Ap + Zrn + Mnz. The chemical evolution of monzogranite from high ( $\sim 71$  wt%) to low ( $\sim 65$  wt%)  $SiO_2$  may reflect entrainment of peritectic minerals from the source (i.e., Cpx + Grt + Pl + Ilm) and/or a mixing with a mantle-derived melt. The evolution of the quartz monzodiorite from  $\sim 54$  to  $\sim 60$  wt%  $SiO_2$  is likely the consequence of fractionation of a cumulate made of Pl + Bt + Cpx and mixing with a felsic magma with a probable monzogranitic composition.

#### U mineralization

Most of the U deposits in the Pontivy-Rostrenen complex ( $\sim 2000$  t of U extracted; IRSN 2004) are spatially associated with the equigranular leucogranite facies (Fig. 3). They are generally localized close to contact with the sedimentary country rock, or to micaschist enclaves (Marcoux 1982; Alabosi 1984; Cuney 2006). The most important U deposits occur as polyphase, commonly hematized, quartz veins mostly oriented N170° and interpreted as tension gashes accommodating dextral wrenching along the SASZ (Marcoux 1982; Alabosi 1984) such as the Bonote ( $\sim 400$  t U extracted) or the Kerlech-Lignol deposits ( $\sim 1000$  t U extracted; Fig. 3). A second type of U deposit, with a main orientation of N120–130°, occurs generally as brecciated quartz veins, such as in the Guern area where  $\sim 40$  t U was extracted (e.g., Quistiave and Kerroch deposits), in relation with second-order faults which also likely developed due to deformation along the SASZ (Marcoux 1982; Alabosi 1984). The third type corresponds to episyenite-hosted deposits such as in the Prat Mérien and Poulprio area ( $\sim 100$  t U extracted; Fig. 3), where the mineralized bodies follow N130–160° oriented faults (Alabosi 1984). The episyenitization of leucogranite during hydrothermal alteration resulted in the dissolution of magmatic quartz, the destabilization of plagioclase, the development of secondary muscovite, and the geodic crystallization of adularia, quartz, montmorillonite, and carbonate, U being disseminated in clay or major minerals (Alabosi 1984). A fourth type of deposits occurs as fracture fillings within Brioverian micaschist xenoliths (e.g., Kerségalec; Cuney 2006) (Fig. 3).

## Analytical techniques

### Whole-rock major and trace elements analyses

Three samples of episyenites collected by Alabosi (1984) in the Prat Mérien and Poulprio quarries (Fig. 3) were crushed in the Géosciences Rennes Laboratory using agate mortars. Chemical analyses were performed by the Service d'Analyse des Roches et des Minéraux (SARM; CRPG-CNRS, Nancy, France) using an ICP-AES for major elements and an ICP-MS for trace elements following the techniques described in Carignan et al. (2001). The results of the whole-rock analyses are provided in Table 1.

### Apatite chemistry and U-Pb dating

Apatite crystals from the different magmatic facies forming the complex as well as an episyenite sample were separated using classical magnetic and heavy liquid methods in the Géosciences Rennes Laboratory. Apatite grains were handpicked under a binocular microscope before being embedded in epoxy resin and polished. Apatite grains were imaged by cathodoluminescence (CL) using a Reliotron CL system in Géosciences Rennes (5 kV acceleration voltage and 600  $\mu$ A beam current) and a Cambridge Image Technology (CITL) Mark 5 CL system at the University of Mons, Belgium (15 kV acceleration voltage and 500  $\mu$ A beam current). The CL system at UMons is also equipped with a CITL COS8200 fiber-based optical spectrometer with a 350–1100-nm spectral range and 4-nm resolution. Spectral calibration was performed with a standard Hg-Ar lamp. The spectra were not corrected for total system response. Backscattered electron (BSE) images and chemical maps were performed using the Cameca SX-100 electron probe micro analyzer (EPMA) at IFREMER (Plouzané, France). Analyses were performed using a 15-keV accelerating voltage and a beam diameter of 15  $\mu$ m. Beam currents of 10 and 20 nA were used for spot analyses and elemental mapping, respectively. Standards were apatite (F K $\alpha$ , TAP crystal, counting time of 30 s; P K $\alpha$ , LPET, 60 s; Ca K $\alpha$ , PET, 30 s), albite (Si K $\alpha$ , TAP, 30 s; Na K $\alpha$ , TAP, 30 s), strontianite (Sr L $\alpha$ , TAP, 30 s), pyromorphite (Cl K $\alpha$ , LPET, 60 s), Si-Al-Ca glass with 4 wt% La (La L $\alpha$ , LPET, 30 s), barium sulfate (S K $\alpha$ , PET, 30 s), Si-Al-Ca glass with 4 wt% Ce (Ce L $\alpha$ , PET, 60 s), andradite (Fe K $\alpha$ , LLIF, 60 s), rhodonite (Mn K $\alpha$ , LLIF, 60 s), and gallium arsenide (As L $\alpha$ , TAP, 60 s).

U-Pb geochronology of apatite was conducted by in situ laser ablation inductively coupled plasma mass spectrometry (LA-ICP-MS) at Géosciences Rennes using a ESI NWR193UC excimer laser coupled to a quadrupole Agilent 7700 $\times$  ICP-MS equipped with a dual pumping system to enhance sensitivity. The methodology used to perform the analyses can be found in Pochon et al. (2016) and in Electronic

**Table 1** Whole-rock major and trace elements composition of episyenite samples

Location		Sample		
		MS-81-66 Prat Mérien (PM)	MS-81-32 Poulprio (PP)	MS-81-40
SiO <sub>2</sub>	wt%	62.97	55.95	58.24
Al <sub>2</sub> O <sub>3</sub>	wt%	17.55	19.84	21.14
Fe <sub>2</sub> O <sub>3</sub>	wt%	4.40	3.01	1.64
MnO	wt%	0.04	0.03	0.03
MgO	wt%	1.00	1.85	1.18
CaO	wt%	1.68	1.04	0.98
Na <sub>2</sub> O	wt%	2.67	0.39	2.42
K <sub>2</sub> O	wt%	4.77	8.59	9.08
TiO <sub>2</sub>	wt%	0.13	0.43	0.39
P <sub>2</sub> O <sub>5</sub>	wt%	1.19	0.49	0.65
LOI	wt%	4.13	8.23	4.08
Total	wt%	100.52	99.85	99.82
Li	ppm	91	70	66
Cs	ppm	17.2	22.8	20.2
Rb	ppm	355	544	582
Sn	ppm	4.0	15.9	15.7
W	ppm	0.89	3.02	2.47
Ba	ppm	528	645	657
Sr	ppm	53.5	46.0	56.1
Be	ppm	8.1	34.4	8.2
U	ppm	113.20	48.42	16.53
Th	ppm	0.59	18.04	14.61
Nb	ppm	2.92	12.30	7.97
Ta	ppm	0.50	2.53	1.67
Zr	ppm	41.3	178.1	157.8
Hf	ppm	1.32	5.61	4.88
Bi	ppm	2.44	0.65	0.78
Cd	ppm	0.41	0.14	0.15
Co	ppm	7.05	1.48	3.25
Cr	ppm	14.72	9.44	8.31
Cu	ppm	25.55	bdl	7.17
Ga	ppm	24.3	30.7	32.4
Ge	ppm	1.18	1.37	1.20
In	ppm	bdl	0.52	0.14
Mo	ppm	bdl	bdl	bdl
Ni	ppm	15.54	bdl	bdl
Pb	ppm	52.1	30.5	25.4
Sc	ppm	3.36	3.71	2.94
Sb	ppm	2.40	2.23	5.07
V	ppm	22.0	22.5	16.0
Y	ppm	44.34	10.91	14.10
Zn	ppm	29.43	31.29	53.36
As	ppm	95.15	20.08	54.01
La	ppm	8.13	30.40	27.24
Ce	ppm	23.90	60.93	58.68

**Table 1** (continued)

		Sample		
		MS-81-66 Prat Mérien (PM)	MS-81-32 Poulprio (PP)	MS-81-40
Location				
Pr	ppm	3.94	7.47	7.18
Nd	ppm	18.02	28.40	28.45
Sm	ppm	5.77	6.85	7.61
Eu	ppm	1.11	0.83	1.12
Gd	ppm	5.89	5.42	6.31
Tb	ppm	1.14	0.68	0.83
Dy	ppm	7.79	2.92	3.59
Ho	ppm	1.65	0.41	0.50
Er	ppm	4.45	0.84	1.00
Tm	ppm	0.66	0.11	0.13
Yb	ppm	4.35	0.68	0.77
Lu	ppm	0.61	0.10	0.11

LOI loss on ignition, *bdl* below detection limit

Material ESM 1. Ages, calculated using the ISOPLOT software (Ludwig 2001), are provided with their  $2\sigma$  uncertainties. All the isotopic ratios as well as the corresponding U and Pb contents in parts per million are provided in ESM 2.

### Uranium oxide U-Pb dating

Petrography and imaging of selected polished thin sections and mounts of uranium oxide samples were carried out at the GeoRessources Laboratory (Nancy, France) and the Centre de Recherches Pétrographiques et Géochimiques (CRPG, Nancy, France). U-Pb dating was carried out at the CRPG by secondary ion mass spectrometry (SIMS). The U oxide samples were first examined using reflected light microscopy. We then selected chemically homogeneous area with high radiogenic lead content suitable for SIMS analyses based on BSE images obtained using a JEOL J7600F, a HITACHI S-4800 (GeoRessources), or a JEOL 6510 (CRPG) scanning electron microscope and major element analyses obtained using a CAMECA SX100 EPMA (GeoRessources). U-Pb isotope analyses were performed using a CAMECA IMS 1270 SIMS. The complete methodology is described in ESM 3. Due to the common Pb-rich character of the U oxides ( $50 < {}^{206}\text{Pb}/{}^{204}\text{Pb} < 11,000$ ), a common lead correction based on the measured  ${}^{204}\text{Pb}$  content and the Pb isotopic composition calculated using the model of Stacey and Kramers (1975) at the estimated age of the U oxide was applied to the analyses. All the isotopic ratios are provided in ESM 4 and ages, calculated using the ISOPLOT software (Ludwig 2001), are provided with their  $2\sigma$  uncertainties.

## Results

### Uranium oxide petrography

Uranium oxide U-Pb dating was performed on six mounts or thin sections belonging to the AREVA collection from the Kerlech (Lignol), Rosglas and Quérrien (Kerjean) deposits as well as three deposits in the region of Guern (Fig. 3: Quistiave, Kerroch, and a sample referenced as “undifferentiated-Guern” in the AREVA collection).

In the Guern region, the mineralization is described as brecciated quartz veins, following N120–130° oriented faults, which mostly occur in tectonized contacts between the porphyritic and equigranular leucogranites close to micashists enclaves and/or small stocks of quartz monzodiorites (Marcoux 1982; Cuney 2006) (Fig. 3). The Quistiave deposit consists of two veins orientated WNW-ESE and dipping SW, occurring about 80 m apart. The veins are more or less parallel to alternating bands of a porphyritic biotite-rich-muscovite granite and an equigranular muscovite-rich and biotite-poor leucogranite, and minor pegmatite veins. The uranium mineralization occurs as discontinuous lenses along these structures and has been mined to a depth of 95 m. The wall zone of the vein is made by a ~1-cm-thick quartz comb where U oxide nodules (up to 50 cm in diameter) have grown. The center part was, then, filled by brecciated quartz, chalcopyrite, galena, sphalerite, marcasite, covellite, and bismuthinite (Cuney 2006). The analyzed sample corresponds to a nodule of pseudo-spherulitic to spherulitic U oxide (Ur1) brecciated by microfractures mainly filled with quartz, chalcopyrite, galena, sphalerite, and a product of alteration of Ur1 (Alt Ur1; Fig. 4a). In the sample from the Kerroch deposit, the mineralization occurs as clusters of millimeter-sized spherulitic U oxides disseminated in a leucogranitic granitic country rock and crosscut by ~10- $\mu\text{m}$ -wide veins filled with quartz and sulfides (Fig. 4b). In the last sample from the Guern region (undifferentiated-Guern, Fig. 4c), 0.05- to 2-mm-wide veins filled by quartz and spherulitic to pseudo-spherulitic U oxide crosscut the leucogranitic country rock.

In the Kerlech (Lignol) deposit, 50-cm- to 1-m-wide mineralized quartz veins oriented N-S to N°170 crosscut the equigranular leucogranite from the contact with the sedimentary rocks (Marcoux 1982; Cuney 2006) (Fig. 3). Vein filling began with a quartz comb followed by fine-grained quartz bearing U oxide and chalcopyrite. The last infilling event is represented by barren quartz (Cuney 2006). In the studied sample, a centimeter large cluster of U oxide spherules (Ur1) up to 500  $\mu\text{m}$  in length occurs in fine-grained (< 1 mm) quartz together with Fe oxides. The first generation of spherulitic U oxide (Ur1) is brecciated by a second generation of U oxide (Ur2) accompanied by quartz, galena, and locally bismuthinite (Fig. 4d).



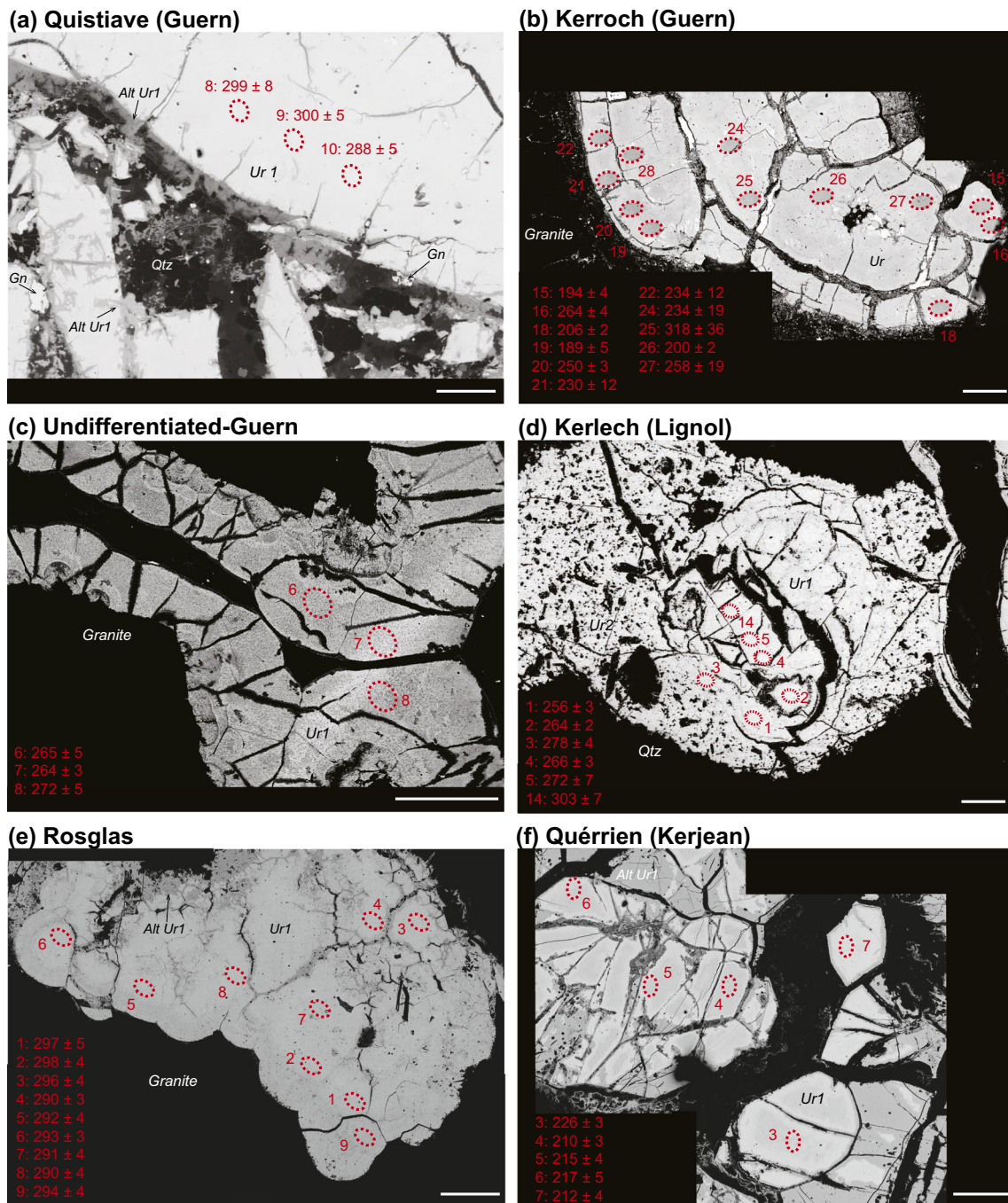


**Fig. 4** Backscattered electron images for uranium oxides (Ur) from U deposits of the Pontivy-Rostrenen district. **a** Pseudo-spherulitic U oxide crosscut by a fracture filled with quartz, alteration product of U oxide (Alt Ur1), and galena (Quistiave deposit). **b** Spherulitic U oxide nodule from the Kerroch deposit. The nodule that occurs inside a granitic country-rock is crosscut by several veinlets filled with sulfides. **c** Vein of pseudo-spherulitic U oxide inside a granitic country rock (undifferentiated-Guern). **d** U oxide in a quartz vein from the Kerlech

deposit. The first generation of spherulitic U oxide (Ur1) was brecciated by quartz and a second generation of U oxide (Ur2). **e** Cluster of U oxide spherules occurring inside a granitic country rock (Rosglas deposit). **f** U oxides from the Qu errien (Kerjean) deposit. Dark gray zones (alt Ur1) correspond to the alteration of the first generation of U oxide. Red dashed ellipses represent the location of SIMS U-Pb analyses with the corresponding  $^{207}\text{Pb}/^{206}\text{Pb}$  age. The white bar represents 100  $\mu\text{m}$

Rosglas and Qu errien (Kerjean) are both classified as episyenite-type deposits and are found in the equigranular leucogranite facies (Fig. 3). At Rosglas, the episyenite forms a nearly cylindrical subvertical column at the intersection of two

faults. In the Rosglas sample, the mineralization occurs as millimeter large clusters of U oxide spherules, with a diameter of 10 to 100  $\mu\text{m}$ , disseminated in episyenitized leucogranitic country rocks (Fig. 4e). In the Qu errien (Kerjean) sample, the

mineralization occurs as brecciated millimeter-wide pseudospherulitic U oxides veinlets or clusters disseminated in episyenitized leucogranitic country rocks. In the BSE images, U oxides, crosscut by numerous millimeter-wide fractures, are characterized by the presence of light gray zones interpreted as unaltered (Ur1) and dark gray zones interpreted as altered U oxide (Alt Ur1; Fig. 4f).

### Uranium oxide U-Pb dating

Chemically, homogeneous areas that had undergone little or no postcrystallization alteration were selected for U-Pb SIMS dating (Fig. 4). Yet, most analyses plot in a discordant position in the Wetherill concordia diagram (Wc) (Fig. 5), suggesting radiogenic Pb losses which could be the result of hydrothermal alteration (Fig. 4).

For the Quistiave (Guern) deposit (Fig. 5a), the eight analyses plot in a discordant position in the Wc diagram and define a poorly constrained upper intercept of  $290 \pm 69$  Ma (MSWD = 4.1) and a lower intercept of  $7 \pm 130$  Ma. If the discordia is anchored at 0 Ma, assuming a recent Pb loss, an upper intercept of  $286 \pm 10$  Ma (MSWD = 3.5) is obtained. For the Kerroch (Guern) deposit (Fig. 5b), the 30 analyses are discordant to concordant and display an important scattering in the Wc diagram. A poorly constrained upper intercept of  $307 \pm 86$  Ma (MSWD = 1.3) and a lower intercept of  $89 \pm 66$  Ma are obtained. For the last sample from the Guern region deposits (Guern-undifferentiated; Fig. 5c), the 15 discordant analyses, affected by Pb loss, define a relatively well-constrained upper intercept of  $268 \pm 8$  Ma (MSWD = 1.2) and a lower intercept of  $-15 \pm 24$  Ma in the Wc diagram. Assuming a recent Pb loss, an upper intercept of  $273 \pm 3$  Ma (MSWD = 1.2) can be calculated. For the Kerlech (Lignol) deposit (Fig. 5d), the 13 analyses plot in a discordant position and display an important scattering in the Wc diagram. The data define a poorly constrained upper intercept of  $258 \pm 89$  Ma (MSWD = 1.3) and a lower intercept of  $-18 \pm 210$  Ma. If the discordia is anchored at 0 Ma in the Wc diagram, an upper intercept of  $267 \pm 11$  Ma (MSWD = 1.2) is obtained. Regarding the sample from the Rosglas deposit (Fig. 5e), the 12 discordant analyses, affected by Pb loss, define a relatively well-defined upper intercept of  $303 \pm 32$  Ma (MSWD = 0.5) and a lower intercept of  $33 \pm 130$  Ma. A comparable upper intercept of  $296 \pm 4$  Ma (MSWD = 0.5) is obtained by anchoring the discordia at 0 Ma. Finally, for the Qu errien (Kerjean) deposit, the 14 analyses plot in concordant to discordant positions in the Wc diagram reflecting no or moderate Pb loss (Fig. 5f). The data define a well-constrained upper intercept of  $219 \pm 5$  Ma (MSWD = 0.9) with a lower intercept of  $-8 \pm 69$  Ma. By anchoring the discordia at 0 Ma, an identical upper intercept of  $219 \pm 5$  Ma (MSWD = 0.8) is obtained.

### Whole-rock geochemistry and U-Th distribution

Some major element compositions of whole-rock samples from the Pontivy-Rostrenen complex are reported in the Q-P diagram (Fig. 6a). Leucogranite, monzogranite, and quartz monzodiorite plot mostly in the field defined for granite-adamellite, ademellite, and quartz monzodiorite, respectively, whereas the episyenite sample from the Prat M errien deposit plots in the granite field and the two episyenite samples from the Poulprio deposit plot out of the field defined for magmatic rocks. The episyenites, which result from leucogranite metasomatism (Alabosi 1984), display evidence of an important dequartzification combined with potassic alteration for Poulprio and a slight dequartzification for Prat M errien (Fig. 6a). Loss on ignition (LOI) between  $\sim 4$  and 8 wt% in the episyenite samples reflects the presence of carbonates and clay minerals (montmorillonite; Alabosi 1984), whereas LOI is below 2 wt% for the unaltered leucogranite. The episyenite sample from Prat M errien is also enriched in  $P_2O_5$  (1.19 wt%; Table 1) compared to other episyenites ( $P_2O_5 < 0.7$  wt%; Table 1) and unaltered leucogranite samples ( $P_2O_5 < 0.5$  wt%; Ballouard et al. 2017b). Moreover, all episyenite samples display higher As content relative to leucogranite with values from 20 to 95 ppm (Table 1) in episyenites, whereas the As content in leucogranite is generally below 11 ppm (Ballouard et al. 2017b).

In the Th versus U diagram (Fig. 6b), monzogranite and quartz monzodiorite samples are characterized by high Th/U values mostly above 3, low U contents from  $\sim 3$  to 9 ppm, and a poorly defined correlation between Th and U. In contrast, the Th/U ratios and U contents are highly variable in the leucogranite and range from  $\sim 0.1$  to 5 and  $\sim 3$  to 27 ppm, respectively. Among leucogranite, the lowest Th/U ratios ( $< 1$ ) and highest U contents ( $> 15$  ppm) are displayed by the equigranular leucogranite and the late equigranular leucogranite, whereas Th/U ratios above 1 and U contents below or equal to 15 ppm are found in the porphyritic leucogranite. U correlates negatively with Th for the late equigranular leucogranite samples, whereas no clear correlation appears for the porphyritic and equigranular leucogranite. In the episyenite, the Th/U ratios range from 0.9 to 0.01 with a U content from 17 to 48 ppm for Poulprio and of 113 ppm for Prat M errien. The Prat M errien episyenite is characterized by an extremely low Th content of 0.6 ppm.

### Apatite petrogeochemistry

Apatite is a common accessory mineral in all the magmatic rocks from the Pontivy-Rostrenen complex. In this study, chemical analyses (Table 2) were performed on separated apatite grains from one porphyritic leucogranite (PONT-1, 13 grains), two equigranular leucogranites (PONT-10, 13 grains; PONT-26, 14 grains), the late equigranular leucogranite

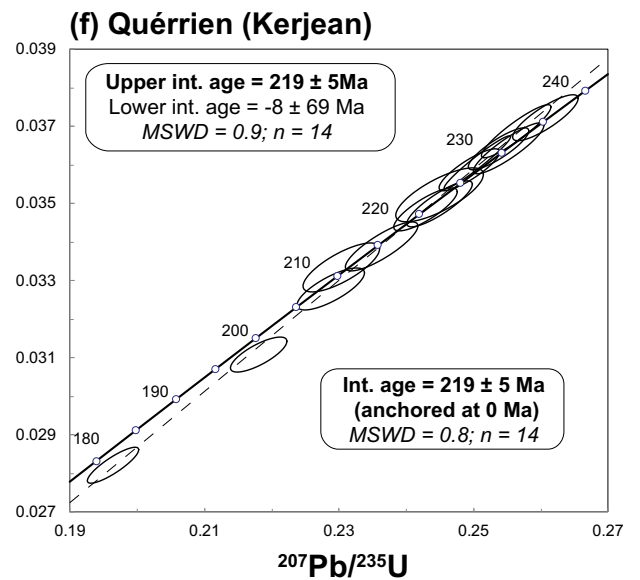
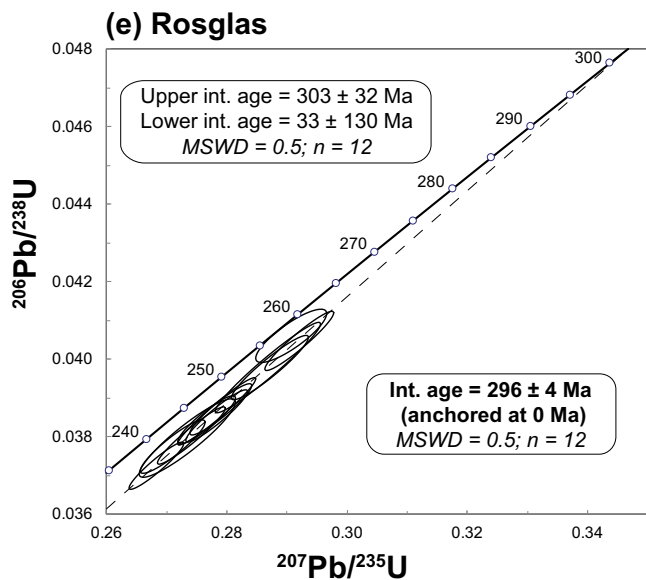
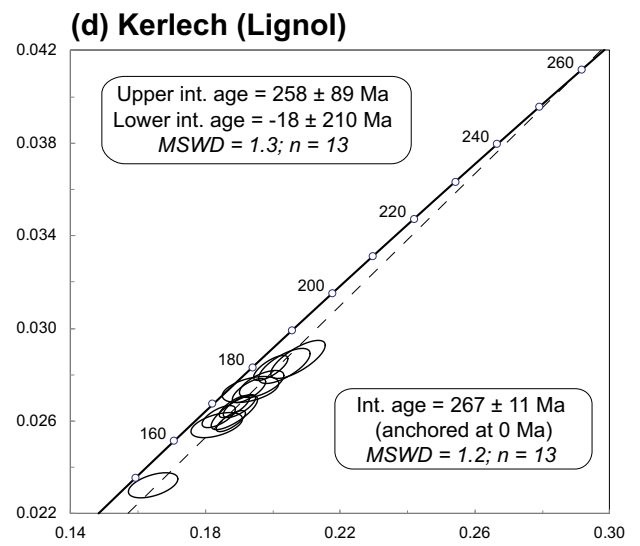
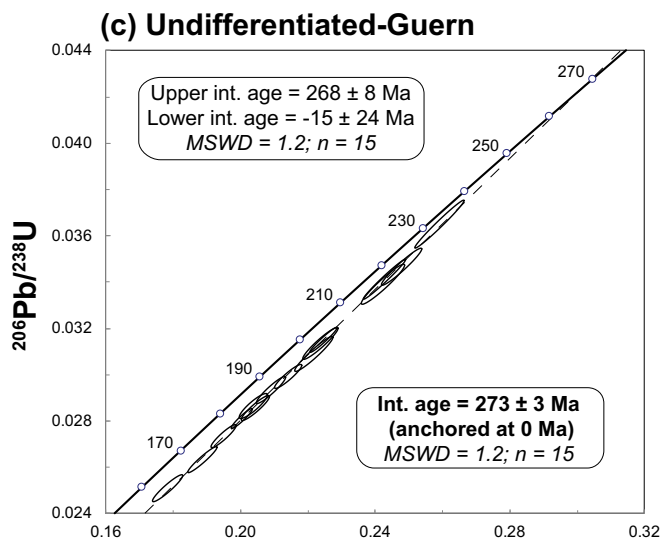
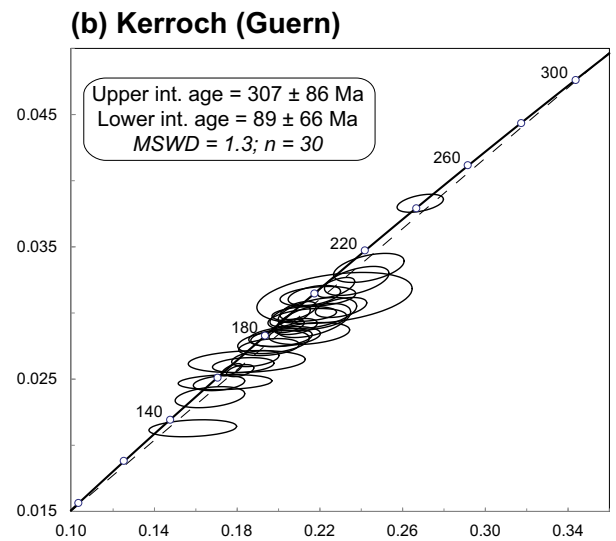
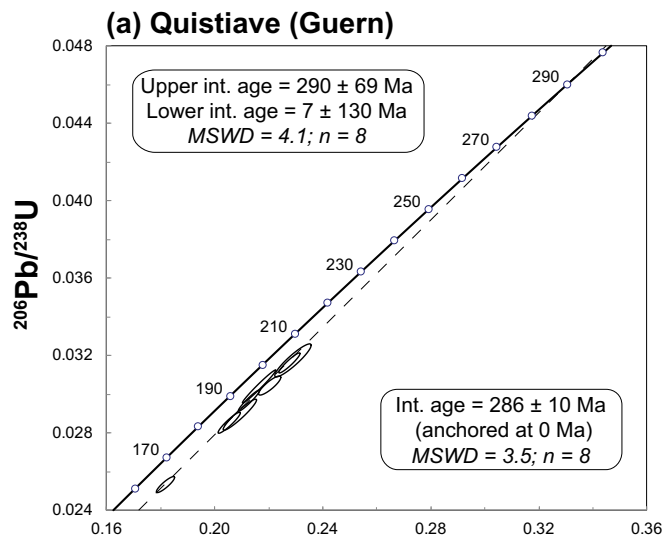


**Fig. 5** Wetherill concordia diagrams displaying the analyses made on uranium oxides from the **a** Quistiave, **b** Kerroch, **c** undifferentiated-Guem, **d** Kerlech, **e** Rosglas, and **f** Quérien U deposits. Ellipses and age errors are reported at  $2\sigma$ . Ages in bold are interpreted as the best estimate for U oxide crystallization

(PONT-20, 13 grains), one episyenite (MS-81-66-PM, 10 grains), one monzogranite (PONT-22, 20 grains), and two quartz-monzodiorites (PONT-7, 14 grains; PONT-23, 15 grains). In all these samples, the F content in the apatite crystals is always above 0.75 apfu indicating that they are fluoroapatite (Table 2).

In all leucogranite and episyenite samples, apatite grains appear as squat prisms up to 500  $\mu\text{m}$  in length. In leucogranite, the crystals display generally yellow-green colors in CL with irregular patchy zoning (Fig. 7a) not visible in the BSE images. In these CL images, the dark yellow-green color characteristic of the grain cores generally evolves toward light yellow-green or even locally blue colors for the rims. CL emission spectra reveal mainly  $\text{Mn}^{2+}$ - and minor  $\text{REE}^{3+}$ -activated luminescence in both yellow-green zones (Fig. 8a). The change from dark yellow-green to light yellow-green color is associated with a decrease in the Fe and Mn contents in the chemical maps (Fig. 7a) and in the Mn versus Fe diagram (Fig. 9), suggesting that the decrease of the CL intensity is due to quenching of Mn-activated CL by Fe or self-quenching effect by Mn (Kempe and Götze 2002). In samples PONT-10 and 26, the cores are characterized by Mn and Fe contents

from 0.04 to 0.17 and 0.02 to 0.07 apfu, respectively, whereas in the rims, the Mn and Fe contents range from < 0.01 to 0.11 and < 0.01 to 0.06 apfu, respectively (Fig. 9). In the episyenite samples, apatite crystals commonly display irregular zoning with yellow-green, blue, blue-gray, or red-pink colors in CL images (Fig. 7b). Blue-gray CL zones are commonly observed as overgrowth or as patches and veins in yellow-green and blue zones, whereas red-pink zones are observed as late overgrowth for the other zones (Fig. 7b). CL spectra reveal mainly  $\text{Mn}^{2+}$  with minor  $\text{Eu}^{2+}$ - and  $\text{REE}^{3+}$ -activated luminescence in yellow-green zones, whereas the CL activation by both  $\text{Eu}^{2+}$  and  $\text{REE}^{3+}$  increases in the other zones (Fig. 8b). As seen on the spectra, the differences in CL color in these apatite grains result from subtle changes in the emission caused by three main activators:  $\text{Eu}^{2+}$  (blue),  $\text{Mn}^{2+}$  (yellow-green), and  $\text{Sm}^{3+}$  (red). Interestingly, the CL spectra in blue, blue-gray, and red-pink zones commonly show activation by  $\text{Eu}^{3+}$  (Fig. 8b). Crystals or zones with a yellow-green color in the CL images are generally characterized by elevated Mn and Fe contents from 0.08 to 0.12 and 0.03 to 0.04 apfu, respectively, whereas blue (and blue-gray) CL zones display Fe and Mn contents < 0.01 apfu (Fig. 9). In contrast, the REE content as indicated by La and Ce concentration does not significantly change (Table 2), suggesting that the increased REE activation in blue and blue-gray CL zones relative to yellow-green CL zones is not due to an increase in REE concentration but rather to a decrease in  $\text{Mn}^{2+}$ . Zones with a red-pink color in CL images

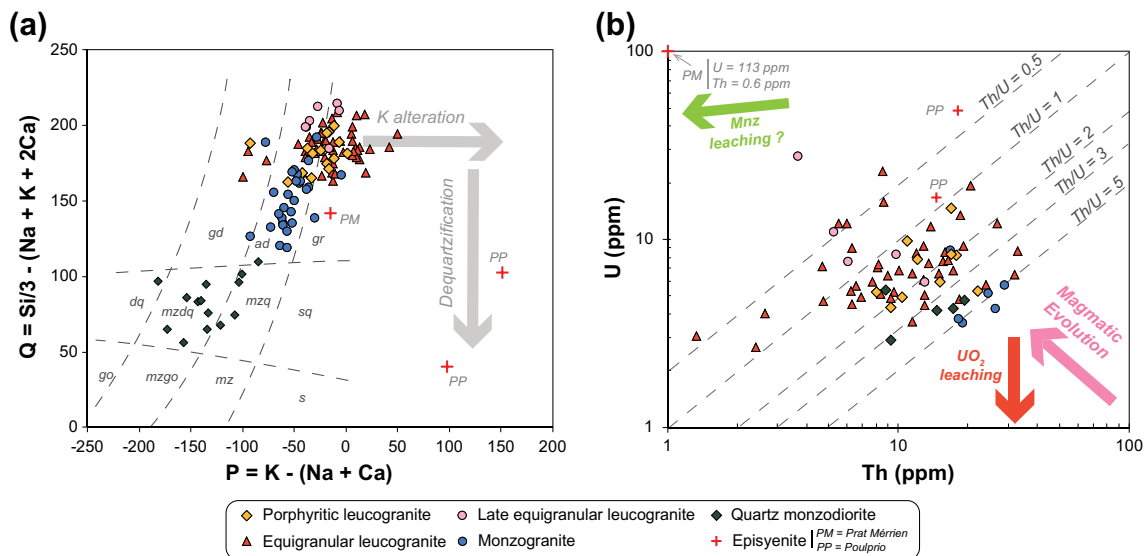


**Fig. 6** Geochemical diagrams showing the whole-rock compositions of samples from the Pontivy-Rostrenen magmatic complex. **a** Q-P diagram (after Debon and Le Fort 1988) where the dashed fields delimit the location of common igneous rock—gr: granite, ad: adamellite (monzogranite), gd: granodiorite, to: tonalite, sq: quartz syenite, mzq: quartz monzonite, mzdo: quartz monzodiorite, s: syenite, mz: monzonite, mzgo: monzogabbro, go: gabbro. Q-P parameters are expressed in molar proportion multiplied by 1000. The gray arrows represent the

compositional evolution of leucogranite during episyenitization. **b** U versus Th diagram where the pink arrow represents the theoretical evolution of a peraluminous leucogranitic melt during fractional crystallization and the red and green arrows represent the evolution of a sample during uranium oxide ( $\text{UO}_2$ ) and monazite (Mnz) leaching, respectively. The sample compositions are from Ballouard et al. (2017b), Cotten (1975), Alabosi (1984), Euzen (1993), Béchenec et al. (2006), Béchenec and Thiéblemont (2011), and Tartèse et al. (2012)

**Table 2** Average chemical composition of apatite

Facies	Por. leucogranite		Equigranular leucogranite											
Sample	PONT-1		PONT-10				PONT-26							
Location			Core		Rim		Unzoned		Core		Rim		Unzoned	
Color CL	Yellow-green		Yellow-green		Yellow-green		Yellow-green		Yellow-green		Yellow-green		Yellow-green	
Analyses	<i>n</i> = 15	$\sigma$	<i>n</i> = 9	$\sigma$	<i>n</i> = 8	$\sigma$	<i>n</i> = 5	$\sigma$	<i>n</i> = 11	$\sigma$	<i>n</i> = 13	$\sigma$	<i>n</i> = 7	$\sigma$
CaO	52.42	0.71	51.97	0.44	53.17	0.55	53.16	0.91	53.21	0.39	54.19	0.73	53.95	0.45
SrO	bdl		bdl		bdl		bdl		bdl		bdl		bdl	
FeO	0.65	0.21	0.65	0.20	0.34	0.20	0.51	0.26	0.56	0.16	0.34	0.19	0.26	0.19
MnO	1.08	0.30	1.89	0.30	1.13	0.28	1.10	0.49	0.84	0.16	0.55	0.29	0.48	0.26
Na <sub>2</sub> O	0.10	0.05	0.06	0.03	0.04	0.03	0.03	0.03	0.09	0.04	0.06	0.04	0.04	0.03
P <sub>2</sub> O <sub>5</sub>	41.74	0.44	41.78	0.39	41.64	0.43	41.70	0.19	41.77	0.24	41.99	0.37	42.02	0.34
SiO <sub>2</sub>	0.01	0.01	0.02	0.01	0.01	0.01	0.02	0.02	0.01	0.02	0.02	0.02	0.03	0.02
SO <sub>2</sub>	0.01	0.02	0.02	0.02	0.01	0.01	0.02	0.02	0.01	0.01	0.01	0.02	0.02	0.02
As <sub>2</sub> O <sub>3</sub>	bdl		0.01	0.01	0.01	0.01	0.01	0.02	bdl		0.01	0.01	0.01	0.01
Ce <sub>2</sub> O <sub>3</sub>	0.07	0.05	0.09	0.05	0.07	0.04	0.05	0.04	0.06	0.04	0.03	0.03	0.06	0.05
La <sub>2</sub> O <sub>3</sub>	0.03	0.03	0.02	0.02	0.01	0.01	0.02	0.04	0.01	0.02	0.02	0.02	0.02	0.02
Cl	0.012	0.007	0.003	0.003	0.008	0.006	0.008	0.003	0.004	0.003	0.005	0.005	0.002	0.003
F	3.316	0.101	3.311	0.107	3.318	0.066	3.235	0.123	3.286	0.093	3.342	0.095	3.385	0.108
Total	99.46	0.84	99.83	0.51	99.76	0.57	99.89	0.42	99.85	0.26	100.56	0.45	100.29	0.37
O = F	1.40	0.04	1.39	0.04	1.40	0.03	1.36	0.05	1.38	0.04	1.41	0.04	1.43	0.05
O = Cl	0.00	0.00	0.00	0.00	0.00	0.00	0.00	0.00	0.00	0.00	0.00	0.00	0.00	0.00
Total*	98.06	0.81	98.43	0.49	98.36	0.58	98.52	0.41	98.47	0.25	99.15	0.44	98.86	0.36
Structural formula on the basis of a 12.5 oxygen equivalent														
Ca	4.80	0.05	4.75	0.04	4.86	0.05	4.85	0.08	4.86	0.03	4.91	0.06	4.90	0.03
Sr	0.00	0.00	0.00	0.00	0.00	0.00	0.00	0.00	0.00	0.00	0.00	0.00	0.00	0.00
Fe	0.05	0.02	0.05	0.01	0.02	0.01	0.04	0.02	0.04	0.01	0.02	0.01	0.02	0.01
Mn	0.08	0.02	0.14	0.02	0.08	0.02	0.08	0.03	0.06	0.01	0.04	0.02	0.03	0.02
Na	0.02	0.01	0.01	0.00	0.01	0.00	0.00	0.00	0.02	0.01	0.01	0.01	0.01	0.00
P	3.02	0.02	3.02	0.01	3.01	0.01	3.01	0.01	3.01	0.01	3.01	0.02	3.01	0.01
Si	0.00	0.00	0.00	0.00	0.00	0.00	0.00	0.00	0.00	0.00	0.00	0.00	0.00	0.00
S	0.00	0.00	0.00	0.00	0.00	0.00	0.00	0.00	0.00	0.00	0.00	0.00	0.00	0.00
As	0.00	0.00	0.00	0.00	0.00	0.00	0.00	0.00	0.00	0.00	0.00	0.00	0.00	0.00
Ce	0.00	0.00	0.00	0.00	0.00	0.00	0.00	0.00	0.00	0.00	0.00	0.00	0.00	0.00
La	0.00	0.00	0.00	0.00	0.00	0.00	0.00	0.00	0.00	0.00	0.00	0.00	0.00	0.00
Cl	0.00	0.00	0.00	0.00	0.00	0.00	0.00	0.00	0.00	0.00	0.00	0.00	0.00	0.00
F	0.90	0.02	0.89	0.03	0.90	0.02	0.87	0.03	0.89	0.02	0.89	0.03	0.91	0.03
OH <sup>a</sup>	0.10	0.02	0.11	0.03	0.10	0.02	0.13	0.03	0.11	0.02	0.11	0.03	0.09	0.03
Facies	Late eq. leucogranite		Episyenite				Monzogranite				Quartz monzodiorite			
Sample	PONT-20		MS-81-66 (PM)				PONT-22				PONT-7		PONT-23	
Location			Blue		Red-pink		Yellow-green		Yellow-green		Purple		Purple	
Analyses	<i>n</i> = 17	$\sigma$	<i>n</i> = 11	$\sigma$	<i>n</i> = 4	$\sigma$	<i>n</i> = 4	$\sigma$	<i>n</i> = 23	$\sigma$	<i>n</i> = 14	$\sigma$	<i>n</i> = 15	$\sigma$
CaO	52.41	0.67	54.47	0.30	52.42	0.67	53.03	1.36	53.21	0.63	53.62	0.51	53.87	0.41
SrO	bdl		bdl		0.08	0.01	bdl		bdl		bdl		0.01	0.01
FeO	0.77	0.24	0.01	0.02	0.05	0.03	0.42	0.28	0.23	0.05	0.05	0.02	0.04	0.02
MnO	0.75	0.12	0.03	0.03	bdl		1.04	0.66	0.31	0.04	0.05	0.02	0.04	0.02
Na <sub>2</sub> O	0.12	0.02	0.01	0.01	0.02	0.02	0.08	0.06	0.12	0.02	0.02	0.01	0.02	0.02
P <sub>2</sub> O <sub>5</sub>	42.61	0.29	42.79	0.38	37.15	0.43	42.64	0.37	42.04	0.50	41.63	0.40	41.59	0.59
SiO <sub>2</sub>	0.01	0.01	0.02	0.02	0.02	0.02	0.01	0.02	0.05	0.06	0.48	0.29	0.22	0.13
SO <sub>2</sub>	0.01	0.02	0.01	0.02	0.01	0.02	0.00	0.00	0.01	0.01	0.01	0.02	0.02	0.02

**Table 2** (continued)

As <sub>2</sub> O <sub>3</sub>	bdl		0.11	0.36	5.17	0.49	0.02	0.02	bdl		0.01	0.01	bdl	
Ce <sub>2</sub> O <sub>3</sub>	0.09	0.05	0.03	0.04	0.08	0.04	0.04	0.03	0.03	0.03	0.24	0.15	0.19	0.12
La <sub>2</sub> O <sub>3</sub>	0.03	0.02	0.01	0.01	0.04	0.04	0.03	0.03	0.01	0.01	0.06	0.05	0.07	0.06
Cl	0.011	0.004	0.005	0.005	0.007	0.010	0.078	0.054	0.030	0.009	0.055	0.014	0.090	0.030
F	3.323	0.107	3.377	0.136	2.784	0.114	3.305	0.126	3.395	0.097	3.332	0.094	3.430	0.090
Total	100.14	0.59	100.89	0.37	97.85	1.01	100.68	0.77	99.45	0.71	99.57	0.59	99.58	0.68
O = F	1.40	0.05	1.42	0.06	1.17	0.05	1.39	0.05	1.43	0.04	1.40	0.04	1.44	0.04
O = Cl	0.00	0.00	0.00	0.00	0.00	0.00	0.02	0.01	0.01	0.00	0.01	0.00	0.02	0.01
Total*	98.74	0.58	99.46	0.36	96.68	1.00	99.27	0.75	98.01	0.70	98.15	0.58	98.12	0.65
Structural formula on the basis of a 12.5 oxygen equivalent														
Ca	4.75	0.05	4.89	0.02	5.02	0.02	4.78	0.08	4.86	0.05	4.89	0.06	4.93	0.03
Sr	0.00	0.00	0.00	0.00	0.00	0.00	0.00	0.00	0.00	0.00	0.00	0.00	0.00	0.00
Fe	0.05	0.02	0.00	0.00	0.00	0.00	0.03	0.02	0.02	0.00	0.00	0.00	0.00	0.00
Mn	0.05	0.01	0.00	0.00	0.00	0.00	0.07	0.05	0.02	0.00	0.00	0.00	0.00	0.00
Na	0.02	0.00	0.00	0.00	0.00	0.00	0.01	0.01	0.02	0.00	0.00	0.00	0.00	0.00
P	3.05	0.01	3.04	0.02	2.81	0.02	3.04	0.01	3.03	0.02	3.00	0.02	3.00	0.02
Si	0.00	0.00	0.00	0.00	0.00	0.00	0.00	0.00	0.00	0.01	0.04	0.02	0.02	0.01
S	0.00	0.00	0.00	0.00	0.00	0.00	0.00	0.00	0.00	0.00	0.00	0.00	0.00	0.00
As	0.00	0.00	0.01	0.02	0.28	0.03	0.00	0.00	0.00	0.00	0.00	0.00	0.00	0.00
Ce	0.00	0.00	0.00	0.00	0.00	0.00	0.00	0.00	0.00	0.00	0.01	0.00	0.01	0.00
La	0.00	0.00	0.00	0.00	0.00	0.00	0.00	0.00	0.00	0.00	0.00	0.00	0.00	0.00
Cl	0.00	0.00	0.00	0.00	0.00	0.00	0.01	0.01	0.00	0.00	0.01	0.00	0.01	0.00
F	0.89	0.03	0.90	0.03	0.79	0.03	0.88	0.03	0.91	0.03	0.90	0.03	0.93	0.02
OH <sup>a</sup>	0.11	0.03	0.10	0.03	0.21	0.03	0.11	0.03	0.08	0.03	0.09	0.03	0.06	0.02

Oxide in weight percent; cationic contents in atoms per formula unit

*Bdl* below detection limit, *Por.* Leucogranite porphyritic leucogranite, *Late eq.* leucogranite late equigranular leucogranite

<sup>a</sup> Calculated OH cationic content

are brighter in the BSE images (Fig. 8b) and are characterized by Fe and Mn below detection limit, an elevated average As content of 0.28 apfu (commonly < 0.01 apfu in other grains), and an elevated average OH content of 0.21 apfu (generally around 0.1 in other crystals; Table 2). There is a perfect match between red-pink CL and As-rich bands (Fig. 7b). Incorporation of As in apatite structure likely explains the decrease of CL intensity since As has been reported as a CL inhibitor (Perseil et al. 2000; Kempe and Götze 2002). The combined increase in both As and OH contents marks the evolution toward the johnbaumite end-member [Ca<sub>5</sub>(AsO<sub>4</sub>)<sub>3</sub>(OH)].

In the monzogranite sample, apatite appears as squat or elongated prisms up to 500 μm in length, homogeneous in BSE images and displaying a generally homogeneous yellow-green CL color (Fig. 7c). CL spectra reveal a major Mn<sup>2+</sup> with a moderate REE<sup>3+</sup>-activated luminescence (Fig. 8c). Rarely, apatite grains display a zonation on Si chemical map with a slight decrease of the Si contents from core (~ 0.02 apfu) to rim (< 0.01 apfu) (Fig. 7c). The Mn (0.02–0.03 apfu) and Fe (0.01–0.03 apfu) contents are generally lower than those found in the apatite grains from the leucogranite (Fig. 9). Regarding the quartz monzodiorite samples, apatite crystals appear as squat or elongated prisms up to 200 μm in length. These apatite crystals appear as homogeneous in BSE images and display a predominant purple CL color with purple-green rims (Fig. 7d). CL emission spectra

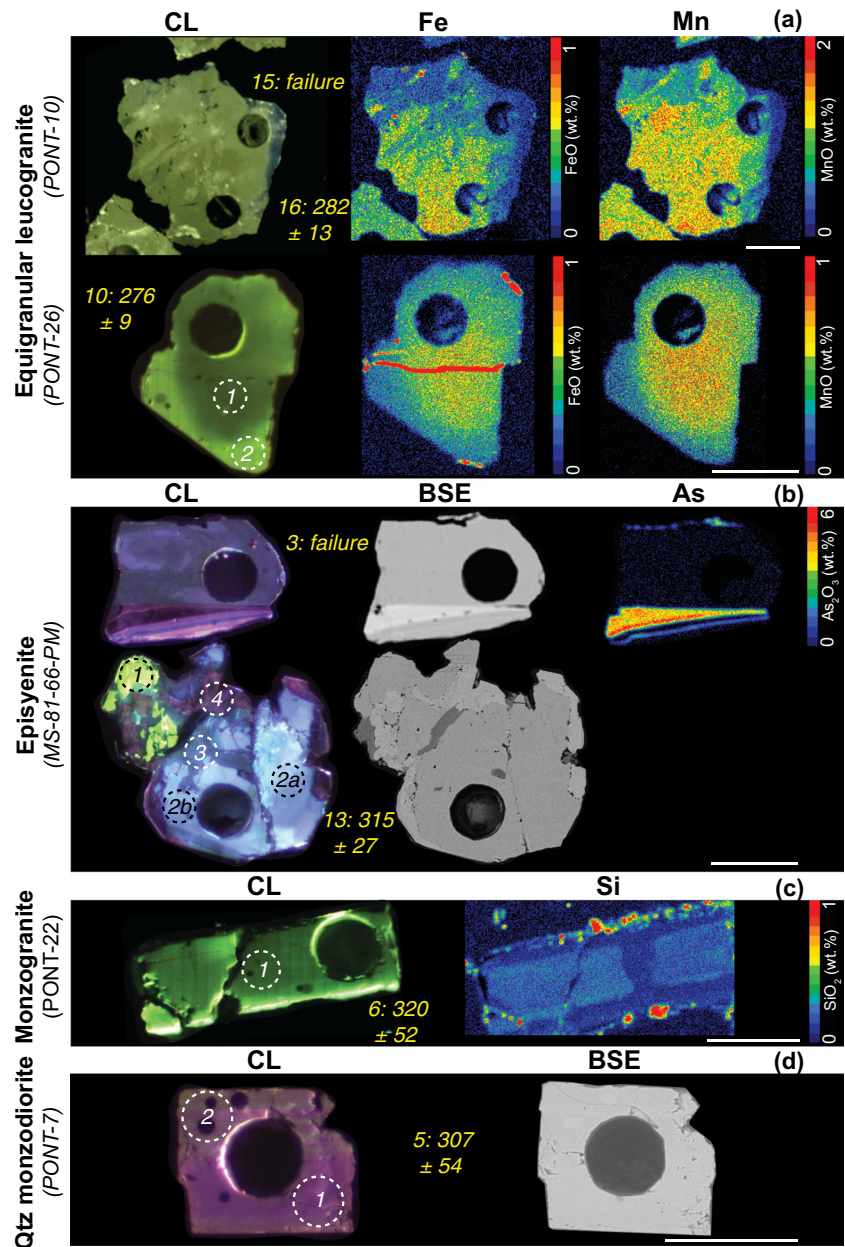
reveal a major REE<sup>3+</sup> and Eu<sup>2+</sup> with minor Mn<sup>2+</sup>-activated luminescence. Here again, slight changes in spectra have an impact on the resulting CL color, with the more greenish CL being induced by a decrease in Sm<sup>3+</sup> (red) relative to Dy<sup>3+</sup> (green). Accordingly, EPMA analyses show a slight decrease of the LREE content ([La + Ce] ~ 0.01 apfu to below detection limits) from core to rim, and these crystals are characterized by low Fe and Mn contents below 0.01 apfu (Fig. 9). Note that here the emission peak at 415 nm (Fig. 8d) could be related to structural defects associated with REE substituting for Ca<sup>2+</sup> (Marshall 1980) as Eu<sup>2+</sup> emission occurs at about 450 nm (e.g., Blanc et al. 2000) as it is the case in episyenite apatite (Fig. 8b).

### Apatite U-Pb dating

Apatite U-Pb analyses were performed for all the samples presented in the last section with the exception of the quartz monzodiorite PONT-23. The results are reported in Tera-Wasserburg diagrams (Fig. 10).

In leucogranite, the analyses are discordant with <sup>207</sup>Pb/<sup>206</sup>Pb ratios ranging from 0.148 to 0.537. Due to the small size of the rims observed in the CL images, analyses were almost exclusively performed on grain cores. For the porphyritic leucogranite sample PONT-1 (Fig. 10a), 23 analyses on 19 different grains define a poorly defined lower intercept of 285.4 ± 8.5 Ma (MSWD = 6.8). Using the common

**Fig. 7** Selected images of apatite grains from magmatic and metasomatic rocks of the Pontivy-Rostrenen complex. **a** Cathodoluminescence (CL) images and chemical maps of Fe and Mn for apatite from leucogranite. **b** CL, backscattered electron (BSE) images and chemical map of As for apatite from an episyenite. **c** CL image and chemical map of Si for apatite from a monzogranite. **d** CL and BSE images for apatite from a quartz-monzodiorite. Numbers in yellow represent the associated <sup>207</sup>Pb-corrected age, whereas dashed circles and associated numbers represent the location of CL emission measurements (Fig. 8). The white bar represents 100 μm



Pb composition calculated at 285 Ma (Stacey and Kramers 1975), the analyses yield two populations for the <sup>207</sup>Pb-corrected ages: 307.2 ± 7.1 Ma (MSWD = 2.2, n = 9) and 286.2 ± 3.8 Ma (MSWD = 1.6, n = 14), respectively. For the equigranular leucogranite sample PONT-10 (18 analyses from 16 grains; Fig. 10b), the unforced discordia yields a lower intercept of 270.4 ± 6.7 Ma (MSWD = 2.5). Once again, two populations are obtained for the corrected <sup>207</sup>Pb ages, calculated using the common Pb composition at 270 Ma, and yield mean values of 294.9 ± 7.4 Ma (MSWD = 0.12) and 279.9 ± 2.9 Ma (MSWD = 0.42), respectively. For the equigranular leucogranite PONT-26 (21 analyses from 15 grains; Fig. 10c), we obtain a lower intercept of 272.8 ± 2.9 Ma (MSWD = 1.2). Two populations of <sup>207</sup>Pb-

corrected ages are obtained and yield mean values of 299.9 ± 4.3 Ma (MSWD = 0.26) and 279.6 ± 2.1 Ma (MSWD = 0.59), respectively. Then, for the late equigranular leucogranite sample (PONT-20; 24 analyses from 18 grains; Fig. 10d), a poorly constrained lower intercept at 278.0 ± 11.0 Ma (MSWD = 8.7) is obtained and analyses yield two populations of <sup>207</sup>Pb-corrected ages with mean values of 297.1 ± 3.0 Ma (MSWD = 1.6) and 280.9 ± 2.1 Ma (MSWD = 0.63), respectively. There is no clear correlation between the apparent <sup>207</sup>Pb-corrected ages obtained for the apatite grains from leucogranite and their relative Mg and/or Fe contents.

For the episyenite sample (MS-81-66-PM; Fig. 10e), the discordant analyses display highly variable common Pb

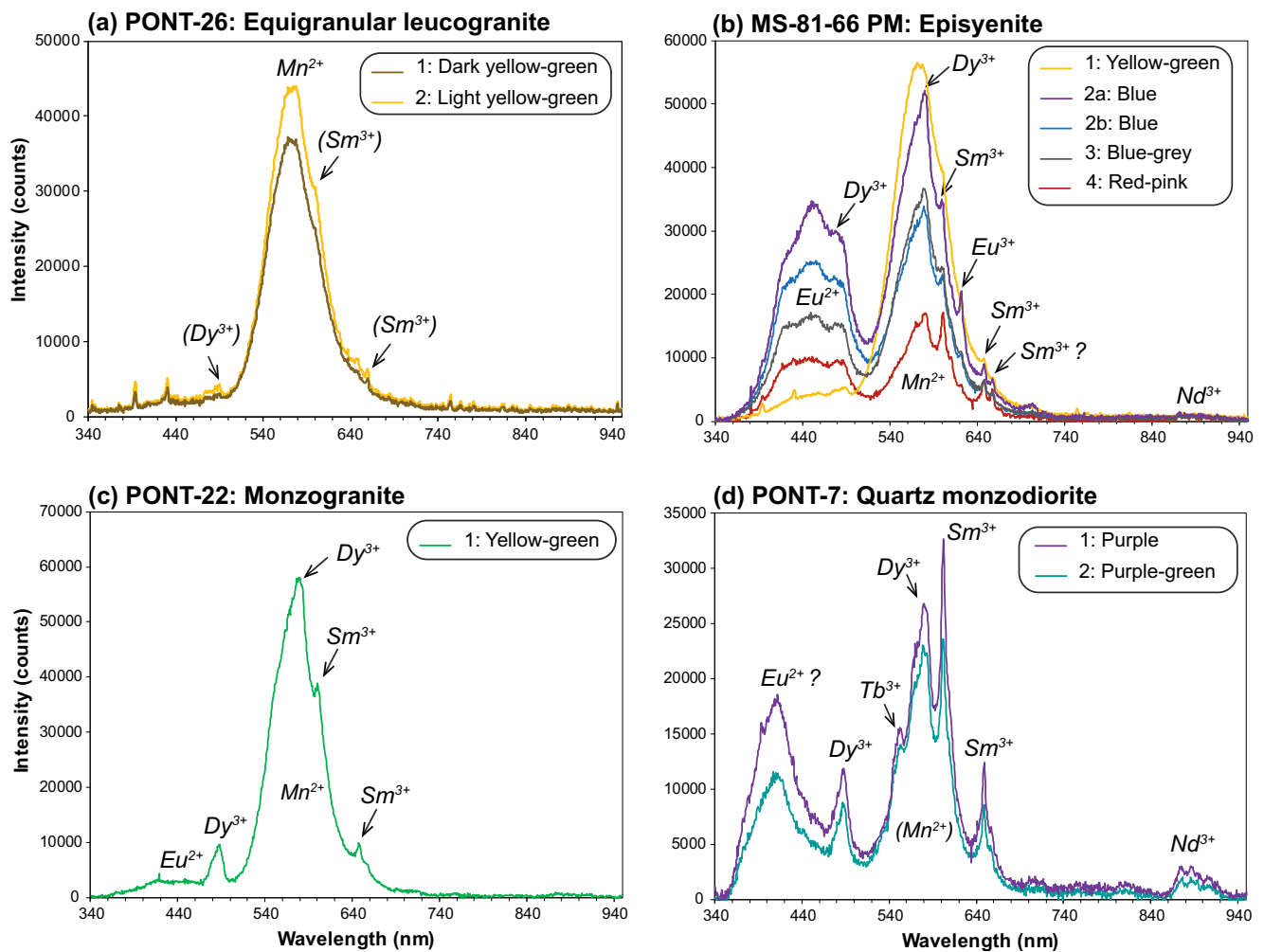
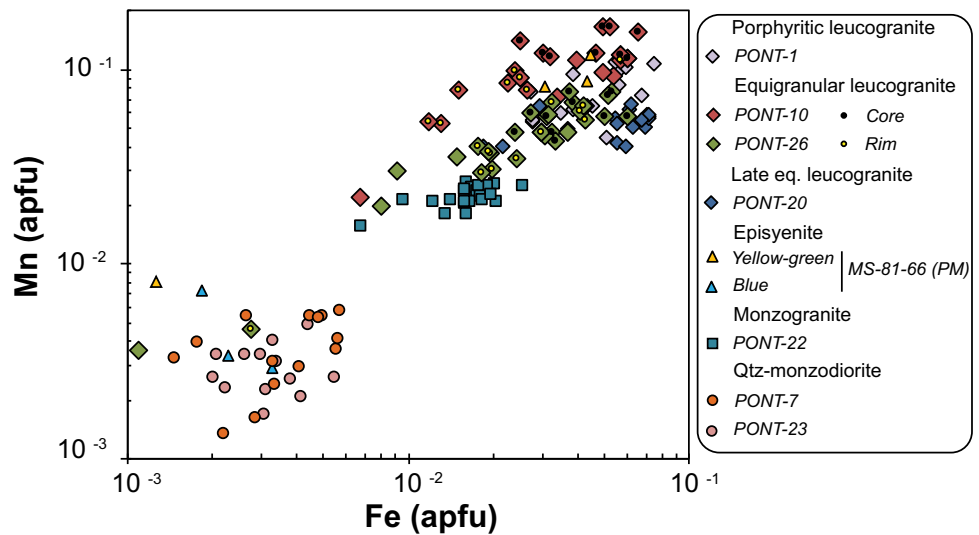


**Fig. 8** Cathodoluminescence emission spectra of representative apatite grains from **a** leucogranite, **b** episyenite, **c** monzogranite, and **d** quartz monzodiorite of the complex. The locations of analyses are indicated in Fig. 7

contents with  $^{207}\text{Pb}/^{206}\text{Pb}$  values ranging from 0.122 to 0.861. No analyses were performed on the blue-gray or pink-red CL

zones because of their small sizes. In this sample, nine analyses out of six grains presenting yellow-green or blue colors

**Fig. 9** Fe versus Mn diagram displaying the EPMA analyses made on apatite grains from the granitoids of the complex. apfu: atoms per formula unit





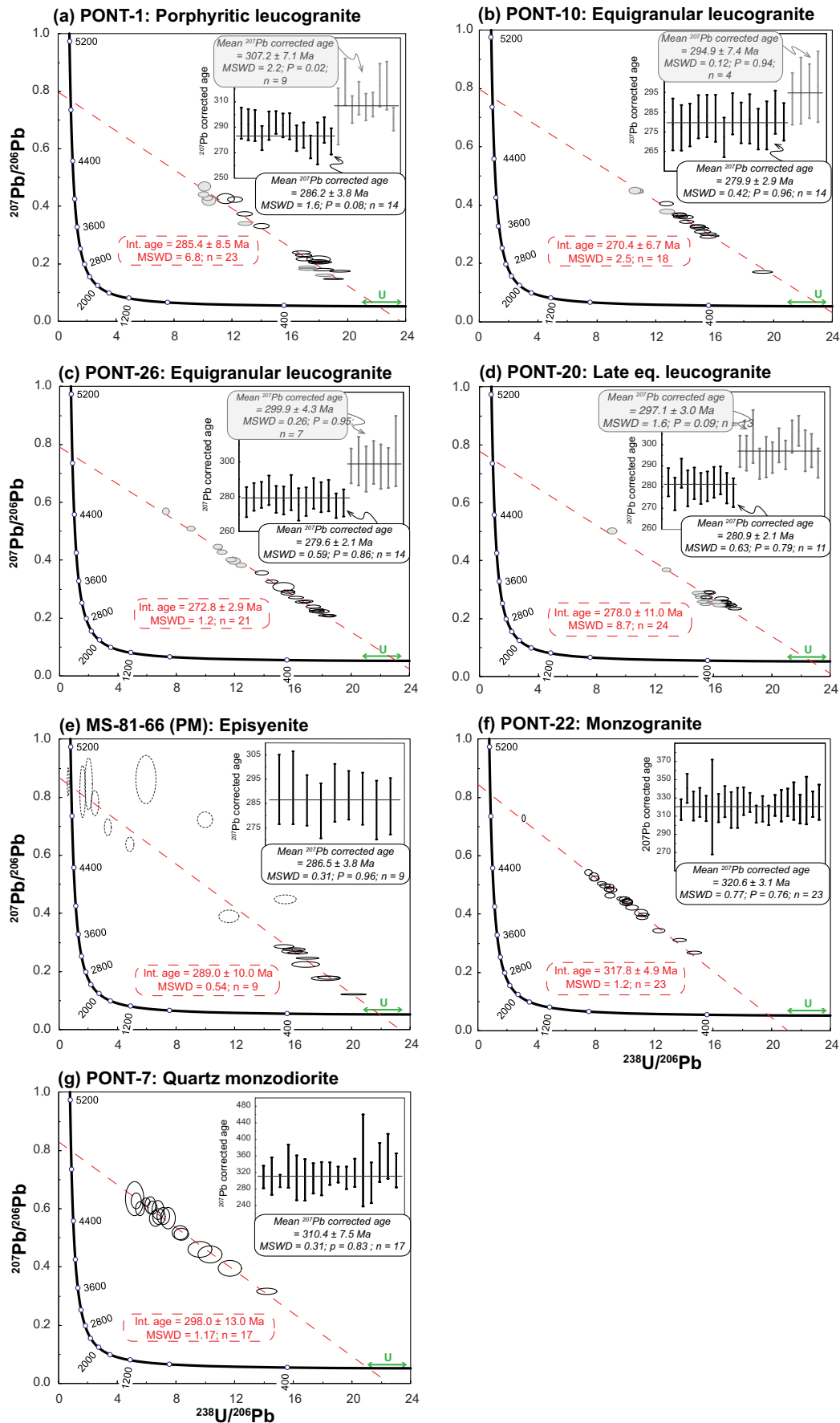


**Fig. 10** Tera-Wasserburg concordia diagrams with the corresponding  $^{207}\text{Pb}$ -corrected ages for LA-ICP-MS analyses made on apatite grains from **a** porphyritic leucogranite, **b–c** equigranular leucogranite, **d** late equigranular leucogranite, **e** episyenite, **f** monzogranite, and **g** quartz monzodiorite of the complex.  $^{207}\text{Pb}$ -corrected ages are calculated using the common Pb composition at the lower intercept age (Stacey and Kramers 1975). Dashed ellipses in **e** represent analyses not used for age calculations. Ellipses and errors on ages are reported at  $2\sigma$ . The main period of U deposit formation in the complex is reported for comparison (green double arrow)

and characterized by  $^{207}\text{Pb}/^{206}\text{Pb}$  values below 0.300 display a well-defined discordia and yield a lower intercept of  $289.0 \pm 10.0$  Ma (MSWD = 0.54). This age is identical within error to the mean  $^{207}\text{Pb}$ -corrected age of  $286.5 \pm 3.8$  Ma (MSWD = 0.31). The other data characterized by a higher common Pb content are more scattered and were therefore not used.

Regarding the monzogranite sample (PONT-22; Fig. 10f), the 23 analyses from 22 grains are discordant with  $^{207}\text{Pb}/^{206}\text{Pb}$  values ranging from 0.268 to 0.729. The analyses yield a well-defined lower intercept of  $317.8 \pm 4.9$  Ma (MSWD = 1.2) identical within error to a mean  $^{207}\text{Pb}$ -corrected age of  $320.6 \pm 3.1$  Ma (MSWD = 0.76).

Finally, for the quartz-monzodiorite sample (PONT-7; Fig. 10g), the 17 analyses from 13 grains are discordant with  $^{207}\text{Pb}/^{206}\text{Pb}$  values from 0.316 to 0.628. The data align on a discordia which yields a well-defined lower intercept of  $298 \pm 13$  Ma (MSWD = 1.17) identical within error to a mean  $^{207}\text{Pb}$ -corrected age of  $310.4 \pm 7.5$  Ma (MSWD = 0.31).

## Discussion

### U behavior in the Pontivy-Rostrenen complex

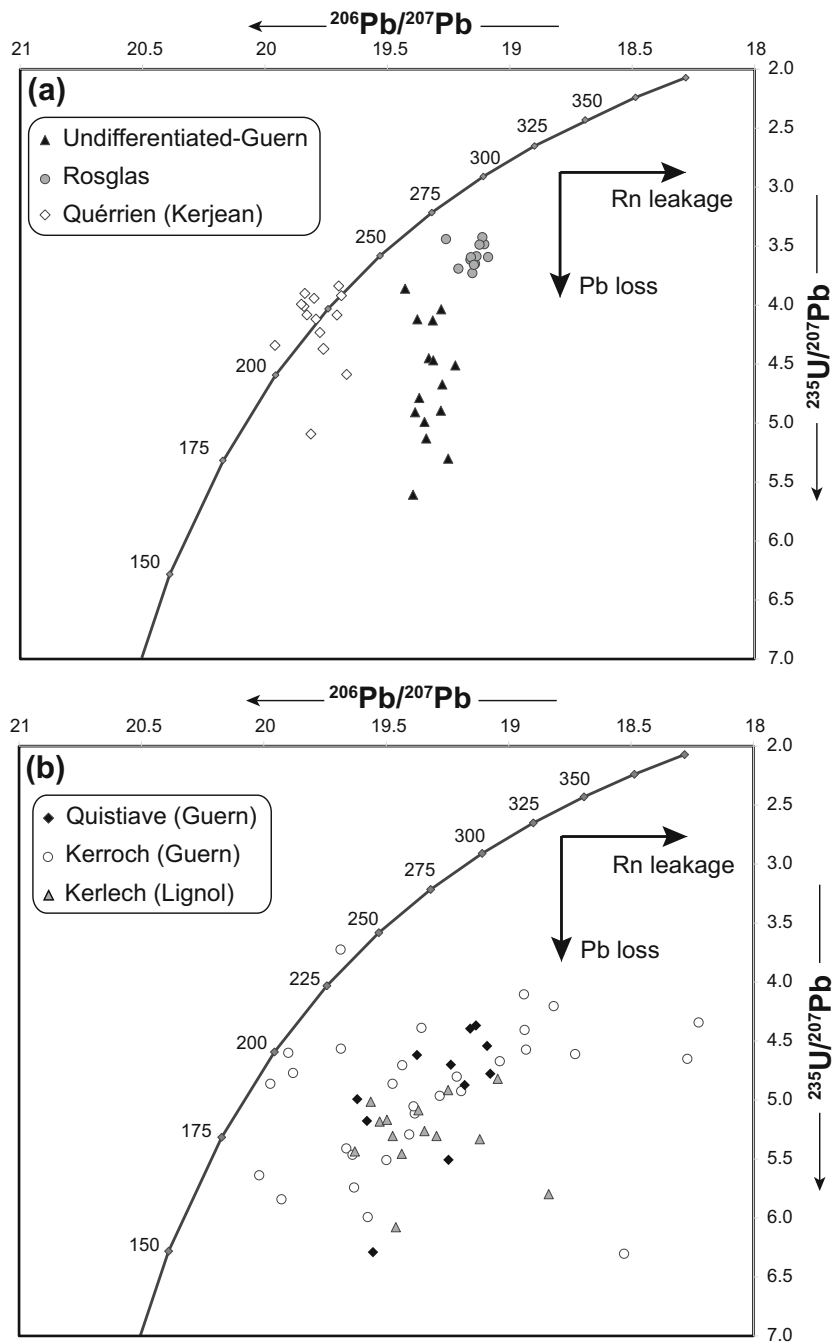
In contrast to the quartz monzodiorite and monzogranite samples, characterized by low U contents (< 9 ppm) and elevated Th/U values mostly above 3, the leucogranite is characterized by both highly variable U contents (~3 to 27 ppm) and Th/U ratios (~0.1 to 5) (Fig. 6b). The Th/U is an indicator of the nature of the U-bearing minerals in granitoids, and the high Th/U ratios (> 2) measured in some samples suggest that most of their U is hosted in refractory mineral phases such as zircon, titanite, or allanite for quartz monzodiorite and zircon or monazite for leucogranite and monzogranite (Cuney 2014). On the other hand, low Th/U values (< 1) and U contents of tens of parts per million in peraluminous leucogranitic melts favor the crystallization of magmatic uranium oxides at the expense of monazite, and up to 80–90% of the available U can be hosted in U oxide (Friedrich et al. 1987; Peiffert et al. 1994, 1996; Förster 1999; Förster et al. 2008; Cuney 2014). In leucogranitic magmas, extraction of accessory minerals

incorporating limited amounts of U, such as monazite and zircon, during fractional crystallization (Ballouard et al. 2017b) likely induced an increase of the U contents in the melts and a decrease of the Th/U values. Such behavior, well-illustrated by the negative correlation between Th and U in the late equigranular leucogranite (Fig. 6b), probably triggered the crystallization of U oxides in the most evolved leucogranitic melts. In contrast, there is no correlation between Th and U for the porphyritic and equigranular leucogranites (Fig. 6b). We propose that the very variable Th/U values displayed by these facies can be attributed to a combination between magmatic evolution (U oxide crystallization), hydrothermal alteration, and/or surface weathering (U oxide leaching), low Th uranium oxides being particularly prone to dissolution by infiltrating oxidized fluids (Förster 1999; Förster et al. 2008). In the episyenite sample, the high U contents suggest hydrothermal U enrichment, while the extremely low Th content of the Prat Mérien sample suggests either a high degree of magmatic fractionation or monazite leaching, the latter being documented in some episyenites (López-Moro et al. 2013).

### Age of the uranium mineralization

U-Pb analyses of uranium oxides provide evidence for a complex behavior of the U-Pb system depending on the samples. A first group composed of the Guern-undifferentiated, Rosglas and Quérrien (Kerjean) samples yield relatively well-constrained, unforced upper intercepts of  $268 \pm 8$ ,  $303 \pm 32$ , and  $219 \pm 5$  Ma, respectively, whereas the Quistiave (Guern), Kerroch (Guern), and Kerlech (Lignol) samples, belonging to the second group, yield poorly constrained unforced upper intercepts of  $290 \pm 69$ ,  $307 \pm 86$ , and  $258 \pm 89$  Ma, respectively (Fig. 5). In Fig. 11, the analyses from the two groups are reported in a  $^{206}\text{Pb}/^{207}\text{Pb}$  versus  $^{235}\text{U}/^{207}\text{Pb}$  concordia diagram that is useful to discriminate between Pb loss and Rn leakage processes in U oxides (Ludwig and Simmons 1992). In this diagram, samples from the first group only display evidence of Pb loss, whereas samples from the second group display evidence for both Pb loss and Rn leakage. It is not possible to constrain precisely the timing of the Rn leakage in these samples, but this process seems to have occurred during the Mesozoic (Fig. 11b). In contrast, unforced lower intercept ages close to 0 suggest recent Pb loss for all samples except Kerroch (Guern; Fig. 5). Therefore, we suggest that the poorly constrained upper intercept U-Pb ages obtained for samples from the second group are the result of a complex combination of Pb loss and Rn leakage. Despite that the Wc diagrams suggest an Upper Carboniferous to Lower Permian age for the crystallization of these samples (Fig. 5), we argue in the following that only the samples

**Fig. 11** a, b  $^{235}\text{U}/^{207}\text{Pb}$  versus  $^{206}\text{Pb}/^{207}\text{Pb}$  concordia diagram displaying the uranium oxide analyses from the uranium deposits of the complex and reporting the theoretical trajectories of uranium daughter loss (Ludwig and Simmons 1992)



from the first group (Fig. 11a) can be used to constrain precisely the timing of the U mineralizing events in the Pontivy-Rostrenen district.

In the Guern region, the Guern-undifferentiated sample yields an unforced upper intercept of  $268 \pm 8$  Ma which is identical within error to the upper intercept of  $273 \pm 3$  Ma obtained if the discordia is anchored at 0 Ma (Fig. 5c). Therefore, we suggest that this deposit formed  $273 \pm 3$  Ma ago. Analyses on uranium oxides from the Rosglas deposit yield an unforced intercept of  $303 \pm 32$  Ma identical within

error to the forced upper intercept age of  $296 \pm 4$  Ma that we interpret as the age of formation (Fig. 5e). Then, the U oxides from the Quérrien (Kerjean) deposit yield two identical well-constrained upper intercepts of  $219 \pm 5$  Ma (Fig. 5f), interpreted as the age of their crystallization. To sum up, the hydrothermal U deposits from the Pontivy-Rostrenen complex mostly formed during the Lower Permian, from ca. 300 to 270 Ma, but some U deposit formation or U remobilization also occurred during the Triassic around 220 Ma as illustrated in the Quérrien (Kerjean) deposit.

## Apatite as a proxy to date emplacement and/or alteration ages?

### *Apatite dating in rocks unaffected by fluids*

In the quartz monzodiorite and the monzogranite, apatite grains are unzoned or display discrete regular zonation on CL images (Fig. 7c, d), which suggest that these crystals have kept their magmatic signature and were not affected by significant hydrothermal processes. U-Pb dating of apatite grains from the quartz monzodiorite yields a lower intercept of  $298.0 \pm 13.0$  Ma identical within error to a mean  $^{207}\text{Pb}$ -corrected age of  $310.4 \pm 7.5$  Ma (Fig. 10g). The mean  $^{207}\text{Pb}$ -corrected age is identical within error to the zircon U-Pb age of  $315.2 \pm 2.9$  Ma obtained for this facies (Ballouard et al. 2017b) (Table 3) and can be interpreted as reflecting the emplacement for this quartz-monzodiorite intrusion. In the monzogranite, apatite grains provide comparable intercept and mean  $^{207}\text{Pb}$ -corrected ages of  $317.8 \pm 4.9$  and  $320.6 \pm 3.1$  Ma (Fig. 10f), respectively. Both ages are identical within error to the zircon U-Pb age of  $315.5 \pm 2.0$  Ma obtained on this sample (Ballouard et al. 2017b) (Table 3) and can be interpreted as reflecting the emplacement age of the intrusion.

### *Apatite dating in rocks affected by fluids*

In contrast to the monzogranite and quartz monzodiorite apatite crystals, the apatite grains from leucogranite and episyenite display petrogeochemical evidence for pervasive hydrothermal alteration. Indeed, these apatite grains show patchy irregular zoning in the CL images and in the Fe and Mn chemical maps, likely reflecting fluid interaction processes (Fig. 7a). The decrease in the Mn and Fe contents, generally observed from the core to the rims (Figs. 7a and 9), likely reflects the transition toward a more oxidized environment during hydrothermal events. Indeed, Mn and Fe are more compatible in apatite in reduced conditions as  $\text{Mn}^{2+}$  and  $\text{Fe}^{2+}$  substitute easily to  $\text{Ca}^{2+}$  (Miles et al. 2014). In addition to the irregular patchy zoning reflecting Fe and Mn mobility, apatite grains from the episyenite also display features likely hydrothermal in origin. The formation of new apatite is in agreement with the elevated whole-rock P content (1.2 wt%) measured for this sample (MS-81-66; Table 1). Late apatite overgrowths, having a red-pink color in CL images, show enrichment in As and OH characteristic of a substitution toward the johnbaumite end-member (Fig. 7b). The observed OH enrichment suggests that these zones crystallized in a  $\text{H}_2\text{O}$ -rich environment, whereas the increase of the As content reflects the high oxygen fugacity of the hydrothermal fluids as  $\text{As}^{5+}$  will substitute more easily for  $\text{P}^{5+}$  than  $\text{As}^{3+}$ . Moreover, apatite zones interpreted as hydrothermal in origin (blue, blue-gray, or red-pink CL zones in episyenite sample MS-81-66; Fig. 7b) show a slight but significant  $\text{Eu}^{3+}$  activation (Fig. 8b)

that could also be interpreted as related to the oxidized character of the mineralizing fluid (Roeder et al. 1987; Mitchell et al. 1997). Roder et al. (1987) argued that no conclusive interpretation regarding the redox state of the fluids can be drawn from the observation of  $\text{Eu}^{3+}$  activation in the CL of apatite because apatite is expected to concentrate preferentially  $\text{Eu}^{3+}$  over  $\text{Eu}^{2+}$ . However, in our episyenite apatite, the involvement of oxidized fluids is supported by the occurrence of  $\text{As}^{5+}$  and the observed  $\text{Eu}^{3+}$  activation could be regarded as an additional evidence.

In the episyenite sample MS-81-66 (Fig. 10e), apatite grains yield a lower intercept of  $289.0 \pm 10$  Ma and a mean  $^{207}\text{Pb}$ -corrected of  $286.5 \pm 3.8$  Ma identical within error. Considering the alteration evidence depicted above, we thus argue that dating of these apatite grains provides the age of the episyenitization (i.e., the metasomatism of the leucogranite) at  $286.5 \pm 3.8$  Ma.

In each of the leucogranite samples, the data obtained by apatite U-Pb dating reveal a complex behavior with regard to their U-Pb system. First of all, the lower intercept obtained for leucogranite are characterized by rather high MSWD values (between 2.5 and 8.7) with the exception of equigranular leucogranite PONT-26 (MSWD = 1.2). This probably means that the scattering of the data can be attributed to geological event(s) rather than to an analytical problem. This is further amplified by the fact that lower intercept and  $^{207}\text{Pb}$ -corrected ages are systematically different and, when available, are always younger than the emplacement ages (Ballouard et al. 2017b; see Table 3). As outlined earlier, all the apatite grains from leucogranite show evidence for some interaction with fluids. At a first order, this means that the U-Pb system in these grains has been affected by late fluid circulations. In all cases, the mean  $^{207}\text{Pb}$ -corrected ages define two different populations for each sample: a first one returning ages in the range  $294.9 \pm 7.4$  to  $307.2 \pm 7.1$  Ma, and a second one with ages ranging from  $279.6 \pm 2.1$  to  $286.2 \pm 3.8$  Ma (Fig. 10a–d). In Fig. 12, the calculated U contents in the apatite grains are reported as a function of the corresponding  $^{207}\text{Pb}$ -corrected ages. Regarding the apatite grains from the monzogranite ([U] ~7–90 ppm), quartz-monzodiorite ([U] ~12–56 ppm), late equigranular leucogranite ([U] ~48–184 ppm), and episyenite ([U] ~95–263 ppm) samples, the U content is relatively constant and there is no correlation with the  $^{207}\text{Pb}$ -corrected ages. In contrast, the U contents in the apatite from the equigranular (and the porphyritic leucogranite) increase as the  $^{207}\text{Pb}$ -corrected ages get younger. This inverse correlation between the apatite grain apparent ages and their U contents likely shows that the fluids which interacted with these apatite grains were U-rich.

In order to determine if we can extract meaningful ages from this dataset, we decided, for each sample, to keep only the population returning the youngest  $^{207}\text{Pb}$ -corrected ages (Fig. 13). The resulting unforced lower intercept ages are

**Table 3** Comparison between the different U-Pb ages obtained on zircon (Ballouard et al. 2017b) and apatite grains from samples of the Pontivy-Rostrenen complex. Ages in bold are interpreted as the best estimate for magma emplacement (monzogranite and quartz monzodiorite) or fluid circulation (leucogranite and episyenite)

Sample	Emplacement age (U-Pb zircon)	Unforced discordia dates	Age used for common Pb	<sup>207</sup> Pb-corrected dates
Porphyritic leucogranite (PONT-1)	316.7 ± 2.5 Ma (MSWD = 1.2)	285.4 ± 8.5 Ma (MSWD = 6.8)	285 Ma	307.2 ± 7.1 Ma <b>286.2 ± 3.8 Ma</b>
Equigranular leucogranite (PONT-10)	310.3 ± 4.7 Ma (MSWD = 2.5)	270.4 ± 6.7 Ma (MSWD = 2.5)	270 Ma	294.9 ± 7.4 Ma <b>279.9 ± 2.9 Ma</b>
Equigranular leucogranite (PONT-26)		272.8 ± 2.9 Ma (MSWD = 1.2)	275 Ma	299.9 ± 4.3 Ma <b>279.6 ± 2.1 Ma</b>
Late eq. leucogranite (PONT-20)	304.7 ± 2.7 Ma (MSWD = 0.57)	278 ± 11 Ma (MSWD = 8.7)	280 Ma	297.1 ± 3 Ma <b>280.9 ± 2.1 Ma</b>
Episyenite (MS-81-66-PM)		289 ± 10 Ma (MSWD = 0.54)	290	<b>286.5 ± 3.8 Ma</b>
Monzogranite (PONT-22)	315.5 ± 2.0 Ma (MSWD = 1.5)	317.8 ± 4.9 Ma (MSWD = 1.2)	315	<b>320.6 ± 3.1 Ma</b>
Monzodiorite Quartzique (PONT-7)	315.2 ± 2.9 Ma (MSWD = 0.94)	298 ± 13 Ma (MSWD = 1.17)	315	<b>310.4 ± 7.5 Ma</b>

*Late eq. leucogranite* late equigranular leucogranite

285.9 ± 7.4 Ma (MSWD = 2.1; PONT-1: porphyritic leucogranite), 266 ± 11 Ma (MSWD = 2.7; PONT-10: equigranular leucogranite), 272.8 ± 6.4 Ma (MSWD = 0.39; PONT-26: equigranular leucogranite), and 278 ± 15 Ma (MSWD = 0.84; PONT-20: late equigranular leucogranite). Individually, all these ages are comparable with their respective mean <sup>207</sup>Pb-corrected ages. We therefore conclude that the youngest mean <sup>207</sup>Pb-corrected ages represent, for each sample, the best estimate of the time when the fluids interacted with the rocks. The other, older, ages probably represent partially reset apatite grains and are therefore meaningless.

As a conclusion, apatite U-Pb dating of episyenite and leucogranite provides evidence for fluid infiltration from ca.

290 Ma (episyenitization) to 275 Ma (late alteration of leucogranite). This period is contemporaneous with the Lower Permian ages obtained on most of the U deposits in the Pontivy-Rostrenen district (Fig. 5). This, together with the fact that the apatite grains affected by the fluids are richer in U than those that have been partly affected, or not affected, suggests that these hydrothermal fluids were the same than those at the origin of the formation of U deposits (Fig. 12).

**Metallogenic model and regional implication**

In the Pontivy-Rostrenen complex, the main U mineralization is hosted in N170° oriented quartz veins (Kerlech-Lignol, Bonote) or as brecciated quartz veins (Guern region) and episyenite bodies (Prat Mérien, Poulprio) where the mineralized zone follows N120–130° and N130–160° oriented brittle lineaments, respectively. As illustrated in Fig. 14 and proposed by Marcoux (1982), the N170° oriented mineralized quartz veins can be interpreted as tension gashes accommodating late dextral movement along the SASZ, whereas the formation of other deposits could be related to second-order faulting also associated with deformation along the SASZ. Muscovite Ar-Ar and zircon or monazite U-Th-Pb dating on syntectonic leucogranite and mylonites from the SASZ (Tartèse et al. 2011b, 2012; Gapais et al. 2015) bracketed the ductile deformation along the SASZ between ca. 315 and 300 Ma. According to uranium oxide and apatite U-Pb dating on U deposits and leucogranite from the Pontivy-Rostrenen complex, respectively, brittle deformation which allowed the mineralizing fluids to circulate was active from ca. 300 to 270 Ma.

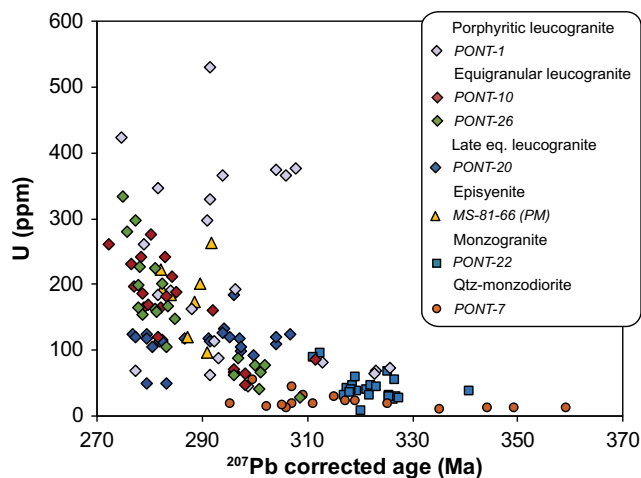


**Fig. 12** Diagram reporting the U content of apatite from the granitoids of the complex as a function of the corresponding <sup>207</sup>Pb-corrected age obtained by LA-ICP-MS

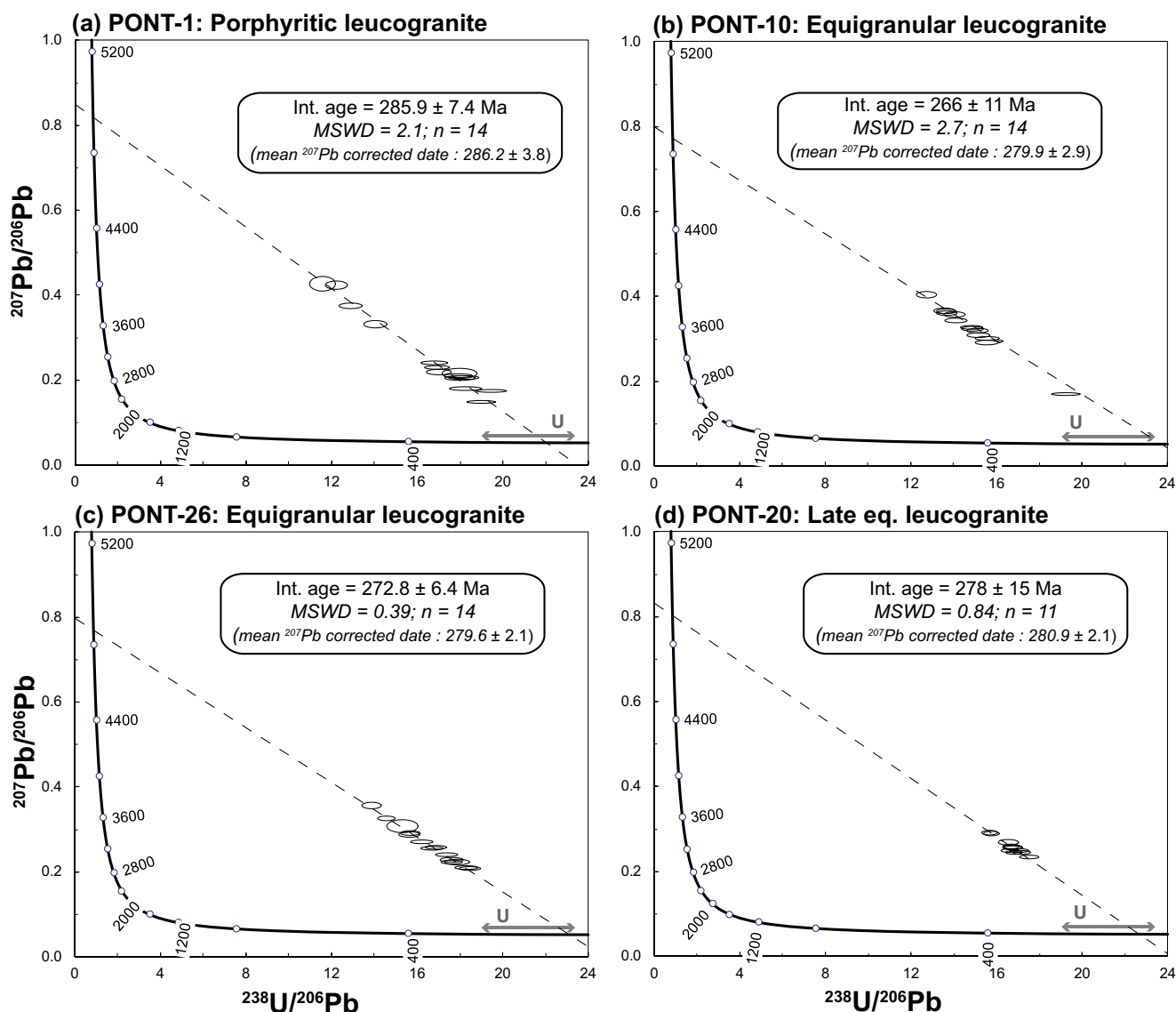


**Fig. 13** Tera-Wasserburg concordia diagrams reporting LA-ICP-MS apatite analyses characterized by young  $^{207}\text{Pb}$ -corrected ages for the **a** porphyritic leucogranite, **b–c** equigranular leucogranite, and **d** late

equigranular leucogranite (Fig. 10). The main period of U deposit formation in the complex is reported for comparison (gray double arrow). Ellipses and age errors are reported at  $2\sigma$

On a regional scale, U deposition in the Pontivy-Rostrenen complex was contemporaneous with U mineralizing events in the Mortagne (from ca. 290 to 260 Ma; Cathelineau et al. 1990) (Fig. 2) and Guérande (from ca. 300 to 275 Ma; Ballouard et al. 2017a; Figs. 2 and 14) districts. In the Guérande district, the main perigranitic vein mineralization (Pen Ar Ran) occurs in a graben structure localized above the apical zone of the Guérande leucogranite. The formation of the graben and U mineralization relates to a brittle-ductile deformation which followed the emplacement of the Guérande intrusion in an extensional setting at ca. 310 Ma (Ballouard et al. 2015, 2017a) (Fig. 14). From 310 to 300 Ma, the SASZ acted as a transfer zone between the South Armorican Massif, a thickened domain in extension, and the Central Armorican Massif, a thin domain under

pervasive dextral wrenching (Gumiaux et al. 2004a; Gapais et al. 2015). According to uranium oxide U-Pb dating, this tectonic configuration was likely active until the middle Permian under mostly brittle conditions. U deposition in the Armorican Massif is contemporaneous with the main U mineralizing phase in the whole EVB (300–260 Ma; Cathelineau et al. 1990; Tischendorf and Förster 1994; Romer et al. 2010; Ballouard et al. 2017a) and follows the main period of formation of W ± Sn granite-related deposits in the Massif Central (Fig. 1) that mostly occurred from ca. 335 to 300 Ma (Harlaux et al. 2017).

As outlined earlier, the apatite grains from leucogranite of the Pontivy-Rostrenen complex and their episyenites show evidence for an interaction with oxidized hydrothermal fluids from ca. 290 to 275 Ma, contemporaneous with the formation

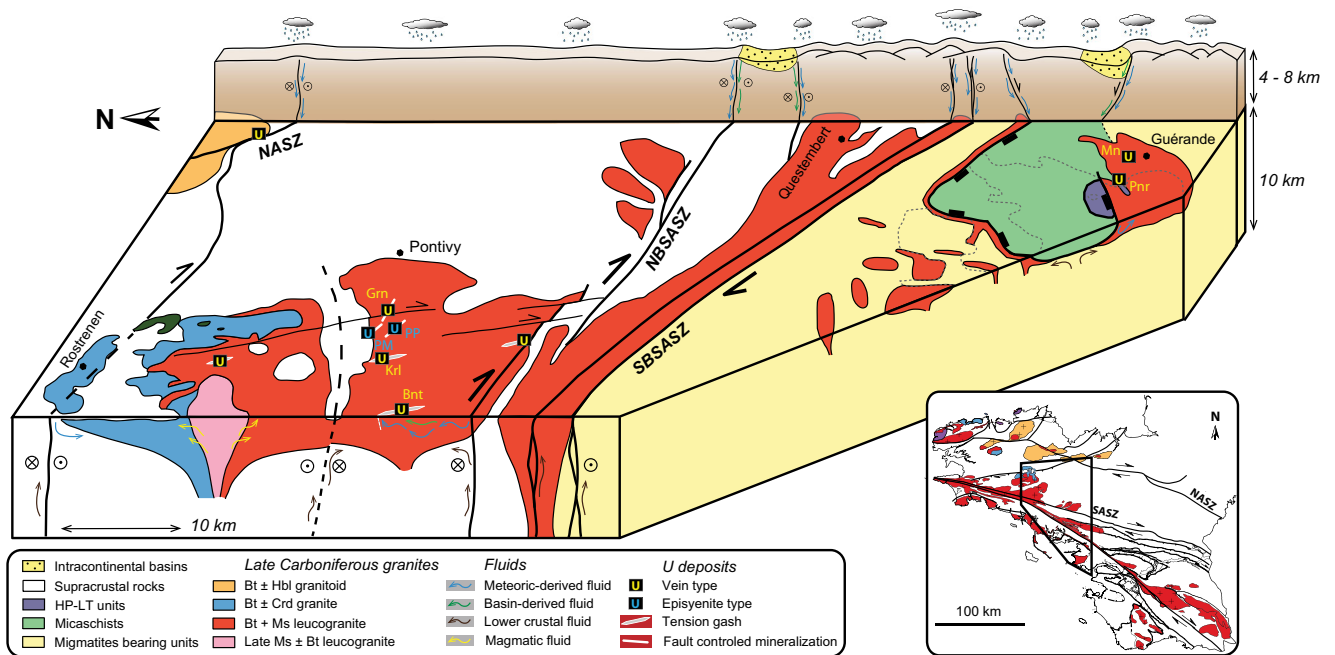


**Fig. 14** Schematic bloc diagram summarizing the geodynamic context of U mineralization formation in the Armorican Variscan belt from 300 to 270 Ma. A schematic cross section representing the topography at the end of the Variscan orogeny is represented in the background. NASZ: north Armorican shear zone, NBSASZ: northern branch of the south

Armorican shear zone, SBSASZ: southern branch of the south Armorican shear zone, Grn: Guern, PP: Poulprio, PM: Prat Mérien, Krl: Kerlech (Lignol), Bnt: Bonote, Mn: Métairie-Neuve, Pnr: Pen Ar Ran. See text for details

of the U deposits. A surface-derived origin is favored as numerous indications for the infiltration of meteoric-derived fluids at depth, from oxygen isotopes and fluid inclusion studies, exist in rocks associated with the SASZ: quartz veins (Lemarchand et al. 2012), leucogranite (Tartèse and Boulvais 2010), and mylonite (Tartèse et al. 2012). For example, a mylonite from the Guillomarch quarry on the southern edge of the Pontivy-Rostrenen complex (Fig. 3) displays whole-rock  $\delta^{18}\text{O}$  values as low as 1.7‰, which indicates interaction with a low  $\delta^{18}\text{O}$  fluid derived from the surface (Tartèse et al. 2012). Surface-derived fluids, likely oxidized, are thus able to transport an important quantity of U in solution (Dubessy et al. 1987). During the Late Carboniferous and Early Permian, the SASZ and the detachments likely acted as major channels for surface-derived oxidized fluids which have the capacity to dissolve magmatic uranium oxides in fertile intrusions such as the Guérande (Ballouard et al. 2017a), Questembert (Tartèse et al. 2013), and Pontivy-Rostrenen leucogranites (Fig. 14).

In the Guérande district (Figs. 2 and 14), fluid inclusion analyses of a quartz from a quartz-uranium oxide vein of the Pen Ar Ran deposit indicate a low salinity mineralizing fluid (1–6 wt% eq. NaCl) with trapping temperatures in the range 250–350 °C (Ballouard et al. 2017a). The trapping temperatures and the salinities of fluid inclusions in the Guérande district are overall comparable with those obtained in U deposits from the Mortagne district (Fig. 2) and the northwestern

part of the Massif Central (Fig. 1), with salinity and temperature generally in the range 0–7 wt% eq. NaCl and 150–250 °C, respectively (Cathelineau 1982; Cathelineau et al. 1990; Lespinasse and Cathelineau 1990; Cuney and Kyser 2008). The low salinity measured in the fluid inclusions from these deposits is in agreement with the contribution of meteoric-derived fluids although the elevated trapping temperatures and the variation of salinity values suggest mixing processes with metamorphic- or basin-derived fluids, as it was already proposed for the FMC (Turpin et al. 1990) and the Bohemian Massif (Křibek et al. 2008; Dolníček et al. 2013).

In the Guérande district, the uranium precipitated at the contact with reducing lithologies, such as black shales (Cathelineau 1981; Ballouard et al. 2017a). In the Pontivy-Rostrenen district, most deposits occurred to the north of the Pontivy intrusion close to the contact with sedimentary country rocks or micaschist enclaves, which likely played a role in the U precipitation processes. In parallel, regional-scale strike-slip faults can act as channels for lower crustal-reduced metamorphic fluids, in addition to surface-derived fluids, such as those documented in regional quartz veins along the SASZ (Lemarchand et al. 2012). These fluids can in turn be involved in U precipitation (Fig. 14). Permian basins are not preserved in the Armorican Massif, with the exception of its northeastern part where shales and red sandstones were deposited in fluvial or lacustrine environments (Ballèvre et al. 2013). However, in the Massif Central, intracontinental basins locally filled by

bituminous shales were proposed as the source of reduced fluids that caused U to precipitate (Turpin et al. 1990; Marignac and Cuney 1999). These Permian basins, that formed during a major episode of extension affecting all western Europe (Kroner and Romer 2013), have a dominant half-graben structural style with a common transtensional character (McCann et al. 2006) attesting for the role of detachments and strike-slip faults in the control of the sedimentation, as illustrated in Fig. 14.

Around 300 Ma, convective fluid infiltration in the Armorican Massif was enhanced by heat from a regional late crustal magmatism event as shown by the emplacement of the late equigranular leucogranite in the Pontivy-Rostrenen district ( $304.7 \pm 2.7$  Ma; Ballouard et al. 2017b) and leucogranitic dykes in the Guérande area ( $302.5 \pm 2.0$  Ma; Ballouard et al. 2015, 2017a). The Permian period in the EVB is marked by an abnormal heat flux in the crust and the mantle, as illustrated, for example, by important granitic magmatism in Cornwall (Chen et al. 1993), in Iberia (Gutiérrez-Alonso et al. 2011), and in Central Europe (Finger et al. 1997; Romer et al. 2007). This heat flux combined with the high heat-producing character of the granites enriched in radioactive elements (Vignerresse et al. 1989) likely sustained an elevated geothermal gradient in the upper crust, able to enhance convective fluid flow (Scaillet et al. 1996). In the Guérande and Pontivy districts, apatite fission tracks dating suggests that leucogranite was at a temperature above 120 °C, or at a depth above 4 km for a geothermal gradient of 30 °C/km, during the formation of the deposits (Fig. 14) (Ballouard 2016; Ballouard et al. 2017a).

Finally, a last U mineralizing or remobilization event occurred at ca. 220 Ma in the Pontivy-Rostrenen district (Rosglas deposit; Figs. 3 and 5f). This mineralizing event is subcontemporaneous with the emplacement of microgabbro dikes in the western part of the Armorican Massif between 210 and 195 Ma which marks the first step of Atlantic rifting (Caroff et al. 1995; Ballèvre et al. 2013). This tectonic event likely caused fluid flow responsible for late, discrete, U mobilization. Triassic and Lower Jurassic U mineralizing or mobilization events are also recorded in the Mortagne district (ca. 200 Ma) and the Massif Central (ca. 210–170 Ma) and have been attributed to the tectonic movements at the origin of the opening of the Tethys (Cathelineau et al. 1990, 2012).

## Conclusion

In the Late Carboniferous Pontivy-Rostrenen composite intrusion, intragranitic hydrothermal U mineralization is associated with the emplacement of peraluminous leucogranite. Mineralization is hosted in quartz veins associated with brittle structures related to strike-slip deformation along the SASZ.

Our study of the U deposits and their magmatic country-rocks leads to the following conclusions:

1. In the peraluminous monzogranite and metaluminous quartz monzodiorite samples, low U contents (<9 ppm) and elevated Th/U values (>3) suggest that most of their U is hosted in refractory minerals such as zircon and monazite for the former and zircon, titanite, and allanite for the latter. For the peraluminous leucogranite, the highly variable U contents (~3–27 ppm) and Th/U ratios (~0.1 to 5) suggest that, in some samples, crystallization of magmatic uranium oxide followed by uranium oxide leaching during subsequent hydrothermal alteration and weathering occurred.
2. Apatite is a powerful tool both for dating and tracing fluids in the system. Apatite grains from the monzogranite and quartz monzodiorite samples are unzoned or display regular zonation in CL images suggesting that these crystals kept their magmatic signature. Apatite U-Pb dating of these samples yields ages around 315 Ma which can be interpreted as emplacement or cooling ages. Apatite grains from leucogranite or episyenite samples display irregular zoning in CL (or BSE) images attributed to the mobility of Fe and Mn or As during an oxidized hydrothermal event involving surface-derived fluids. Apatite U-Pb dating of episyenite and leucogranite samples yields ages from ca. 290 to 275 Ma, interpreted to date the oxidized hydrothermal event. In the leucogranite facies associated with U deposits, the younger apatite grains are enriched in U compared to older ones, suggesting that these oxidized fluids were involved in the formation of U deposits.
3. U-Pb dating of uranium oxide from the U deposits revealed a main Permian U mineralizing phase from 300 to 270 Ma synchronous with the oxidized hydrothermal event recorded by apatite grains from leucogranite. A late U mineralization or remobilization event also occurred during the Triassic at ca. 220 Ma.

On a regional scale, U deposition from 300 to 270 Ma in the Pontivy-Rostrenen complex is contemporaneous with the main U mineralizing phase in the Armorican Massif and the European Variscan belt. During this period, late brittle dextral deformation along the SASZ was synchronous with discrete extension in the South Armorican Domain suggesting a continuum of the ductile deformation which occurred in the region during Late Carboniferous from ca. 315 to 300 Ma. Detachment zones and regional scale strike-slip faults acted as major channels for oxidized surface-derived fluids which were in turn able to dissolve magmatic uranium oxide from fertile peraluminous leucogranite and then form hydrothermal U deposits due to the interaction with reducing lithologies and/or crustal- or basin-derived fluids.



**Acknowledgements** We want to thank AREVA (in particular D. Virlogeux, J.M. Vergeau, and P.C. Guiollard) for providing uranium oxide samples, historical reports, and data and for fruitful discussions. We are grateful to Y. Lepagnot (Geosciences, Rennes) for crushing the samples. Many thanks to J. Langlade (IFREMER, Brest), O. Rouer, S. Matthieu, and L. Salsi (SCMEM - Géoressources, Nancy) for their technical supports during EPMA and SEM analyses. Thank you to N. Bouden (CRPG, Nancy) for the help during SIMS analyses. J.M., M.C., and M.C. would also like to thank AREVA for the permission to publish the present manuscript. This manuscript benefited from the comments of R. Shail and an anonymous reviewer. We want to thank R.L. Romer and G. Beaudoin for editorial handling.

**Funding information** This study was supported by 2012–2013 NEEDS-CNRS and 2015-CESSUR-INSU (CNRS) research grants attributed to M. Poujol.

## References

- Alabosi M (1984) Les altérations hydrothermales associées aux gisements d'uranium de Ty Gallen, Poulprio et Prat Mérien (massif de Pontivy, Morbihan, France). Dissertation, INPL (Institut National Polytechnique de Lorraine), Nancy
- Ballèvre M (2016) Une histoire géologique du Massif armoricain. *Géochronique* 140
- Ballèvre M, Martínez Catalán JR, López-Carmona A, Pitra P, Abati J, Díez Fernández R, Ducassou C, Arenas R, Bosse V, Castiñeiras P, Fernández-Suárez J, Gómez Barreiro J, Paquette JL, Peucat JJ, Poujol M, Ruffet G, Sánchez Martínez S (2014) Correlation of the nappe stack in the Ibero-Armorican arc across the Bay of Biscay: a joint French–Spanish project. *Geol Soc Lond Spec Publ* 405:77–113. <https://doi.org/10.1144/SP405.13>
- Ballèvre M, Bosse V, Dabard MP, Ducassou C, Fourcade S, Paquette JL, Peucat JJ, Pitra P (2013) Histoire Géologique du massif Armoricain: Actualité de la recherche. *Bull Soc Geol Mineral Bretagne (D)* 10-11:5–96
- Ballèvre M, Bosse V, Ducassou C, Pitra P (2009) Palaeozoic history of the Armorican Massif: models for the tectonic evolution of the suture zones. *Comptes Rendus Geosci* 341:174–201. <https://doi.org/10.1016/j.crte.2008.11.009>
- Ballouard C (2016) Origine, évolution et exhumation des leucogranites peralumineux de la chaîne hercynienne armoricaine: implication sur la métallogénie de l'uranium, Dissertation, Université de Rennes 1. <tel.archives-ouvertes.fr/tel-01434903/>
- Ballouard C, Poujol M, Boulvais P, Zeh A (2017b) Crustal recycling and juvenile addition during lithospheric wrenching: the Pontivy-Rostrenen magmatic complex, Armorican Massif (France), Variscan belt. *Gondwana Res* 49:222–247. <https://doi.org/10.1016/j.gr.2017.06.002>
- Ballouard C, Poujol M, Boulvais P, Mercadier J, Tartèse R, Venneman T, Deloule E, Jolivet M, Kéré I, Cathelineau M, Cuney M (2017a) Magmatic and hydrothermal behavior of uranium in syntectonic leucogranites: the uranium mineralization associated with the Hercynian Guérande granite (Armorican Massif, France). *Ore Geol Rev* 80:309–331. <https://doi.org/10.1016/j.oregeorev.2016.06.034>
- Ballouard C, Boulvais P, Poujol M, Gapais D, Yamato P, Tartèse R, Cuney M (2015) Tectonic record, magmatic history and hydrothermal alteration in the Hercynian Guérande leucogranite, Armorican Massif, France. *Lithos* 220–223:1–22. <https://doi.org/10.1016/j.lithos.2015.01.027>
- Béchenec F, Thiéblemont D, Audru JC (2006) Plouay 348, Carte Géologique de France 1:50 000. BRGM
- Béchenec F, Thiéblemont D (2011) Bubry 349, Carte Géologique de France 1:50 000. BRGM
- Berthé D, Choukroune P, Jegouzo P (1979) Orthogneiss, mylonite and non-coaxial deformation of granites: the example of the South Armorican Shear Zone. *J Struct Geol* 1:31–42. [https://doi.org/10.1016/0191-8141\(79\)90019-1](https://doi.org/10.1016/0191-8141(79)90019-1)
- Blanc P, Baumer A, Cesbron F, Ohnenstetter D, Panczer G, Rémond G (2000) Systematic cathodoluminescence spectral analysis of synthetic doped minerals: anhydrite, apatite, calcite, fluorite, scheelite and Zircon. In: Pagel M, Barbin V, Blanc, P, Ohnenstetter D (eds) *Cathodoluminescence in geosciences*, Springer, Heidelberg, pp 127–160
- Bos P, Castaing C, Clément JP, Chantraine J, Lemeille F (1997) Rostrenen 312, Carte Géologique de France 1:50 000. BRGM
- Bosse V, Féraud G, Ballèvre M, Peucat JJ, Corsini M (2005) Rb–Sr and  $^{40}\text{Ar}/^{39}\text{Ar}$  ages in blueschists from the Ile de Groix (Armorican Massif, France): implications for closure mechanisms in isotopic systems. *Chem Geol* 220:21–45. <https://doi.org/10.1016/j.chemgeo.2005.02.019>
- Brown M (2010) The spatial and temporal patterning of the deep crust and implications for the process of melt extraction. *Philos T Roy Soc A* 368:11–51
- Brun JP, Guennoc P, Truffert C, Vairon J (2001) Cadomian tectonics in northern Brittany: a contribution of 3-D crustal-scale modelling. *Tectonophysics* 331:229–246. [https://doi.org/10.1016/S0040-1951\(00\)00244-4](https://doi.org/10.1016/S0040-1951(00)00244-4)
- Capdevila R (2010) Les granites varisques du Massif Armoricain. *Bull Soc Geol Mineral Bretagne* 7:1–52
- Cao S, Neubauer F (2016) Deep crustal expressions of exhumed strike-slip fault systems: shear zone initiation on rheological boundaries. *Earth-Sci Rev* 162:155–176. <https://doi.org/10.1016/j.earscirev.2016.09.010>
- Carignan J, Hild P, Mevelle G, Morel J, Yeghicheyan D (2001) Routine analyses of trace elements in geological samples using flow injection and low pressure on-line liquid chromatography coupled to ICP-MS: a study of geochemical reference materials BR, DR-N, UB-N, AN-G and GH. *Geostand Newslett* 25:187–198. <https://doi.org/10.1111/j.1751-908X.2001.tb00595.x>
- Caroff M, Bellon H, Chauris L, Carron JP, Chevrier S, Gardinier A, Cotten J, Moan YL, Neidhart Y (1995) Magmatisme fissural triasico-liasique dans l'ouest du Massif armoricain (France): pétrologie, géochimie, âge, et modalités de la mise en place. *Can J Earth Sci* 32:1921–1936. <https://doi.org/10.1139/e95-147>
- Cathelineau M (1981) Les Gisements Uranifères de la Presqu'île Guérandaise (Sud Bretagne): Approche Structurale et Métallogénique. *Mineral Deposita* 16:227–240. <https://doi.org/10.1007/BF00202737>
- Cathelineau M (1982) Les gisements d'uranium liés spatialement aux leucogranites sud armoricains et à leur encaissant métamorphique: relations et interactions entre les minéralisations et divers contextes géologiques et structuraux. *Sciences de la Terre, Mémoires* 42. Université de Nancy
- Cathelineau M, Boiron MC, Holliger P, Poty B (1990) Metallogenesis of the French part of the Variscan orogen. Part II: time-space relationships between U, Au and Sn-W ore deposition and geodynamic events—mineralogical and U-Pb data. *Tectonophysics* 177:59–79. [https://doi.org/10.1016/0040-1951\(90\)90274-C](https://doi.org/10.1016/0040-1951(90)90274-C)
- Cathelineau M, Boiron MC, Fourcade S, Ruffet G, Clauer N, Belcourt O, Coulibaly Y, Banks DA, Guillocheau F (2012) A major Late Jurassic fluid event at the basin/basement unconformity in western France:  $^{40}\text{Ar}/^{39}\text{Ar}$  and K–Ar dating, fluid chemistry, and related geodynamic context. *Chem Geol* 322–323:99–120. <https://doi.org/10.1016/j.chemgeo.2012.06.008>
- Cháb J, Stráňík Z, Eliáš M (2007) Geologická mapa České republiky 1: 500 000. Česká geologická služba, Praha, Czech Republic

- Chantraine J, Autran A, Cavalier C (2003) Carte géologique de France 1: 1 000 000 6ème édition révisée. BRGM
- Chauris L (1984) Accidents linéaires et minéralisations uranifères; L'exemple de la ceinture batholitique hercynienne médio-armoricaine (France). *Bull Soc Geol Fr* S7–XXVI:1375–1380. <https://doi.org/10.2113/gssgfbull.S7-XXVI.6.1375>
- Chen Y, Clark AH, Farrar E, Wasteneys HAHF, Hodgson MJ, Bromley AV (1993) Diachronous and independent histories of plutonism and mineralization in the Cornubian Batholith, southwest England. *J Geol Soc* 150:1183–1191. <https://doi.org/10.1144/gsjgs.150.6.1183>
- Civis Llovera J (2015) Mapas geológicos de España y Portugal 1:1 000 000. IGME: Instituto Geológico y Minero de España
- Cotten J (1975) Etude des mégacrists du granite de Rostrenen (Massif Armoricain). Dissertation, Université de Bretagne Occidentale, Brest
- Cuney M (2014) Felsic magmatism and uranium deposits. *Bull Soc Geol Fr* 185:75–92. <https://doi.org/10.2113/gssgfbull.185.2.75>
- Cuney M (2006) Excursion « granites varisques et minéralisations uranifères ». L'exemple des massifs de Ploumanac'h et de Pontivy. Partie II: Métallogenèse de l'uranium. Séminaire AREVA-BUM-DEX
- Cuney M, Kyser TK (2008) Recent and not-so-recent developments in uranium deposits and implications for exploration. *Mineral Assoc Canada Short Course Series* 39
- Cuney M, Friedrich M, Blumenfeld P, Bourguignon A, Boiron MC, Vignerresse JL, Poty B (1990) Metallogenesis in the French part of the Variscan orogen. Part I: U preconcentrations in pre-Variscan and Variscan formations—a comparison with Sn, W and Au. *Tectonophysics* 177:39–57. [https://doi.org/10.1016/0040-1951\(90\)90273-B](https://doi.org/10.1016/0040-1951(90)90273-B)
- D'Lemos RS, Brown M, Strachan RA (1992) Granite magma generation, ascent and emplacement within a transpressional orogen. *J Geol Soc* 149:487–490. <https://doi.org/10.1144/gsjgs.149.4.0487>
- Dadet P, Bos P, Chantraine J, Laville P, Sagon JP (1988) Pontivy 313, Carte Géologique de France 1:50 000. BRGM
- Debon F, Le Fort P (1988) A cationic classification of common plutonic rocks and their magmatic associations: principles, method, applications. *Bull Mineral* 111(5):493–510
- De Saint BM, Tikoff B, Teyssier C, Vignerresse JL (1998) Transpressional kinematics and magmatic arcs. *Geol Soc Lond Spec Publ* 135:327–340. <https://doi.org/10.1144/GSL.SP.1998.135.01.21>
- Dolníček Z, René M, Hermannová S, Prochaska W (2013) Origin of the Okrouhlá Radouň episyenite-hosted uranium deposit, Bohemian Massif, Czech Republic: fluid inclusion and stable isotope constraints. *Mineral Deposita* 49:409–425. <https://doi.org/10.1007/s00126-013-0500-5>
- Dubessy J, Ramboz C, Nguyen Trung C, Cathelineau M, Charoy B, Cuney M, Leroy J, Poty B, Weisbrod A (1987) Physical and chemical control (pO<sub>2</sub>, T, pH) of the opposite behaviour of U and Sn-W as exemplified by hydrothermal deposits in France and Great Britain, and solubility data. *Bull Mineral* 110:262–281
- Euzeu T (1993) Pétrogenèse des granites de collision post-épaississement. Le cas des granites crustaux et mantelliques du complexe de Pontivy-Rostrenen (Massif Armoricain, France). *Mémoires Géosciences Rennes* 51
- Faulkner DR, Jackson CAL, Lunn RJ, Schlische RW, Shipton ZK, Wibberley CAJ, Withjack MO (2010) A review of recent developments concerning the structure, mechanics and fluid flow properties of fault zones. *J Struct Geol* 32:1557–1575
- Finger F, Roberts MP, Haunschmid B, Schermaier A, Steyrer HP (1997) Variscan granitoids of central Europe: their typology, potential sources and tectono-thermal relations. *Mineral Petrol* 61:67–96. <https://doi.org/10.1007/BF01172478>
- Förster HJ (1999) The chemical composition of uraninite in Variscan granites of the Erzgebirge, Germany. *Mineral Mag* 63:239–252. <https://doi.org/10.1180/002646199548466>
- Förster HJ, Rhede D, Hecht L (2008) Chemical composition of radioactive accessory minerals: implications for the evolution, alteration, age, and uranium fertility of the Fichtelgebirge granites (NE Bavaria, Germany). *Neues Jahrb Fr Mineral - Abh J Mineral Geoche* 185:161–182. <https://doi.org/10.1127/0077-7757/2008/0117>
- Friedrich M, Cuney M, Poty B (1987) Uranium geochemistry in peraluminous leucogranites. *Uranium* 3:353–385
- Fusán O, Kodym O, Matějka A et al (1967) Geological map of Czechoslovakia 1:500 000. Czech Geological Survey, Praha
- Gaafar I (2015) Application of gamma ray spectrometric measurements and VLF-EM data for tracing vein type uranium mineralization, El-Sela area, South Eastern Desert, Egypt. *NRIAG J Astron Geophys* 4:266–282. <https://doi.org/10.1016/j.nrjag.2015.10.001>
- Gaafar I, Cuney M, Gawad AA (2014) Mineral chemistry of two-mica granite rare metals: impact of geophysics on the distribution of uranium mineralization at El Sela Shear Zone, Egypt. *Open J Geol* 4: 137–160. <https://doi.org/10.4236/ojg.2014.44011>
- Gapais D (1989) Shear structures within deformed granites: mechanical and thermal indicators. *Geology* 17:1144–1147. [https://doi.org/10.1130/0091-7613\(1989\)017<1144:SSWDGM>2.3.CO;2](https://doi.org/10.1130/0091-7613(1989)017<1144:SSWDGM>2.3.CO;2)
- Gapais D, Brun JP, Gumiaux C, Cagnard F, Ruffet G, Le Carlier De Veslud C (2015) Extensional tectonics in the Hercynian Armorican belt (France). An overview. *Bull Soc Geol Fr* 186:117–129. <https://doi.org/10.2113/gssgfbull.186.2-3.117>
- Gapais D, Lagarde JL, Le Corre C, Audren C, Jegouzo P, Casas Sainz A, Van Den Driessche J (1993) La zone de cisaillement de Quiberon: témoin d'extension de la chaîne varisque en Bretagne méridionale au Carbonifère. *C R Acad Sci, Paris, série II* 316:1123–1129
- Gapais D, Le Corre C (1980) Is the Hercynien belt of Brittany a major shear zone? *Nature* 288:574–576. <https://doi.org/10.1038/288574a0>
- Gébelin A, Roger F, Brunel M (2009) Syntectonic crustal melting and high-grade metamorphism in a transpressional regime, Variscan Massif Central, France. *Tectonophysics* 477:229–243. <https://doi.org/10.1016/j.tecto.2009.03.022>
- Gumiaux C, Judenherc S, Brun JP, Gapais D, Granet M, Poupinet G (2004b) Restoration of lithosphere-scale wrenching from integrated structural and tomographic data (Hercynian belt of western France). *Geology* 32:333–336. <https://doi.org/10.1130/G20134.2>
- Gumiaux C, Gapais D, Brun JP, Chantraine J, Ruffet G (2004a) Tectonic history of the Hercynian Armorican Shear belt (Brittany, France). *Geodin Acta* 17:289–307. <https://doi.org/10.3166/ga.17.289-307>
- Gutiérrez-Alonso G, Fernández-Suárez J, Jeffries TE, Johnston ST, Pastor-Galán D, Murphy JB, Franco MP, Gonzalo JC (2011) Diachronous post-orogenic magmatism within a developing orocline in Iberia, European Variscides. *Tectonics* 30:TC5008. <https://doi.org/10.1029/2010TC002845>
- Harlaux M, Romer RL, Mercadier J, Morlot C, Marignac C, Cuney M (2017) 40 Ma years of hydrothermal W mineralization during the Variscan orogenic evolution of the French Massif Central revealed by U-Pb dating of wolframite. *Mineral Deposita*:1–31. <https://doi.org/10.1007/s00126-017-0721-0>
- Hutton DHW, Reavy RJ (1992) Strike-slip tectonics and granite petrogenesis. *Tectonics* 11:960–967. <https://doi.org/10.1029/92TC00336>
- IRSN (2004) Inventaire national des sites miniers d'uranium. Institut de Radioprotection et de Sureté Nucléaire
- Jégouzo P, Rossello EA (1988) La Branche Nord du Cisaillement Sud-Armoricain (France): un essai d'évaluation du déplacement par l'analyse des mylonites. *C R Acad Sci, Paris, Série II* 307(17): 1825–1831
- Jégouzo P (1980) The South Armorican Shear Zone. *J Struct Geol* 2:39–47. [https://doi.org/10.1016/0191-8141\(80\)90032-2](https://doi.org/10.1016/0191-8141(80)90032-2)
- Judenherc S, Granet M, Brun JP, Poupinet G (2003) The Hercynian collision in the Armorican Massif: evidence of different lithospheric domains inferred from seismic tomography and anisotropy. *Bull Soc Geol Fr* 174:45–57

- Kempe U, Götze J (2002) Cathodoluminescence (CL) behaviour and crystal chemistry of apatite from rare-metal deposits. *Mineral Mag* 66(1):151–172
- Kříbek B, Žák K, Dobeš P, Leichmann J, Pudilová M, René M, Scharm B, Scharmová M, Hájek A, Holeczy D, Hein UF, Lehmann B (2008) The Rožná uranium deposit (Bohemian Massif, Czech Republic): shear zone-hosted, late Variscan and post-Variscan hydrothermal mineralization. *Mineral Deposita* 44:99–128. <https://doi.org/10.1007/s00126-008-0188-0>
- Kroner U, Romer RL (2013) Two plates - many subduction zones: the Variscan orogeny reconsidered. *Gondwana Res* 24:298–329. <https://doi.org/10.1016/j.gr.2013.03.001>
- Lemarchand J, Boulvais P, Gaboriau M, Boiron MC, Tartèse R, Cokinos M, Bonnet S, Jégouzo P (2012) Giant quartz vein formation and high-elevation meteoric fluid infiltration into the South Armorican Shear Zone: geological, fluid inclusion and stable isotope evidence. *J Geol Soc* 169:17–27. <https://doi.org/10.1144/0016-76492010-186>
- Lespinnas M, Cathelineau M (1990) Fluid percolations in a fault zone: a study of fluid inclusion planes in the St Sylvestre granite, northwest Massif Central, France. *Tectonophysics* 184:173–187. [https://doi.org/10.1016/0040-1951\(90\)90052-A](https://doi.org/10.1016/0040-1951(90)90052-A)
- Li JW, Zhou MF, Li XF, Fu ZR, Li ZJ (2002) Structural control on uranium mineralization in South China: implications for fluid flow in continental strike-slip faults. *Sci China Ser Earth Sci* 45:851–864. <https://doi.org/10.1007/BF02879519>
- Li JW, Zhou MF, Li XF, Fu ZR, Li ZJ (2001) The Hunan-Jiangxi strike-slip fault system in southern China: southern termination of the Tan-Lu fault. *J Geodyn* 32:333–354. [https://doi.org/10.1016/S0264-3707\(01\)00033-3](https://doi.org/10.1016/S0264-3707(01)00033-3)
- López-Moro FJ, Moro MC, Timón SM, Cembranos ML, Cózar J (2013) Constraints regarding gold deposition in episyenites: the Permian episyenites associated with the Villalcampo Shear Zone, central western Spain. *Int J Earth Sci* 102:721–744. <https://doi.org/10.1007/s00531-012-0844-6>
- Ludwig KR (2001) Isoplot, a geochronological toolkit for Microsoft Excel. Berkeley Geochronology Center, Spec Publ 5:75
- Ludwig KR, Simmons KR (1992) U-Pb dating of uranium deposits in collapse breccia pipes of the Grand Canyon region. *Econ Geol* 87:1747–1765. <https://doi.org/10.2113/gsecongeo.87.7.1747>
- Marcoux E (1982) Etude géologique et métallogénique du district plombo-zincifère de Pontivy (Massif armoricain, France) : Relations avec les paragenèses stannifères et uranifères. *Bull BRGM* (2), section II, n 1: 1–24
- Marignac C, Cuney M (1999) Ore deposits of the French Massif Central: insight into the metallogenesis of the Variscan collision belt. *Mineral Deposita* 34:472–504. <https://doi.org/10.1007/s001260050216>
- Marshall DJ (1980) Cathodoluminescence of geological materials. Hunwin Hyman
- McCann T, Pascal C, Timmerman MJ, Krzywiec P, López-Gómez J, Wetzel L, Krawczyk CM, Rieke H, Lamarche J (2006) Post-Variscan (end Carboniferous-Early Permian) basin evolution in Western and Central Europe. *Geol Soc Lond Mem* 32:355–388
- Miles AJ, Graham CM, Hawkesworth CJ, Gillespie MR, Hinton RW, Bromiley GD (2014) Apatite: a new redox proxy for silicic magmas? *Geochim Cosmochim Acta* 132:101–119. <https://doi.org/10.1016/j.gca.2014.01.040>
- Mitchell RH, Xiong J, Mariano AN, Fleet ME (1997) Rare-earth-element-activated cathodoluminescence in apatite. *Can Mineralogist* 35:979–998
- Ouddou D (1984) Le Massif de Guérande-Le Croisic (Loire-Atlantique): Caractérisation géochimique et minéralogique de l'évolution magmatique. Comportement de l'uranium, Dissertation, INPL-CREGU Nancy
- Peiffert C, Nguyen-Trung C, Cuney M (1996) Uranium in granitic magmas: part 2. Experimental determination of uranium solubility and fluid-melt partition coefficients in the uranium oxide-haplogranite-H<sub>2</sub>O-NaX (X = Cl, F) system at 770°C, 2 kbar. *Geochim Cosmochim Acta* 60:1515–1529. [https://doi.org/10.1016/0016-7037\(96\)00039-7](https://doi.org/10.1016/0016-7037(96)00039-7)
- Peiffert C, Cuney M, Nguyen-Trung C (1994) Uranium in granitic magmas: part 1. Experimental determination of uranium solubility and fluid-melt partition coefficients in the uranium oxide-haplogranite-H<sub>2</sub>O-Na<sub>2</sub>CO<sub>3</sub> system at 720–770°C, 2 kbar. *Geochim Cosmochim Acta* 58:2495–2507. [https://doi.org/10.1016/0016-7037\(94\)90026-4](https://doi.org/10.1016/0016-7037(94)90026-4)
- Pérez Del Villar L, Moro C (1991) Las mineralizaciones intragraníticas de Uranio en el batolito de Cabeza de Ar aya (provincia de Cáceres): El Saguzal, Brechas NNE y La Zafrilla. *Stud Geol Salmant* 27:85–112
- Perseil EA, Blanc P, Ohnenstetter D (2000) As-bearing fluorapatite in manganiferous deposits from St. Marcel – Praboma, Val d'Aosta, Italy. *Can Mineralogist* 38:101–117
- Pirajno F (2010) Intracontinental strike-slip faults, associated magmatism, mineral systems and mantle dynamics: examples from NW China and Altay-Sayan (Siberia). *J Geodyn* 50:325–346. <https://doi.org/10.1016/j.jog.2010.01.018>
- Pochon A, Poujol M, Gloaguen E, Branquet Y, Cagnard F, Gumiaux C, Gapais D (2016) U-Pb LA-ICP-MS dating of apatite in mafic rocks: evidence for a major magmatic event at the Devonian-Carboniferous boundary in the Armorican Massif (France). *Am Mineral* 101:2430–2442. <https://doi.org/10.2138/am-2016-5844>
- Roeder PL, McArthur D, Ma XP, Palmer GR, Mariano A (1987) Cathodoluminescence and microprobe study of rare-earth elements in apatite. *Am Mineral* 72:801–811
- Romer RL, Schneider J, Linnemann U (2010) Post-Variscan deformation and hydrothermal mineralization in Saxo-Thuringia and beyond: a geochronologic review. In: Linnemann U, Romer RL (eds) *Pre-Mesozoic geology of Saxo-Thuringia—from the Cadomian active margin to the Variscan Orogen*. Schweizerbart, Stuttgart, pp 347–360
- Romer RL, Thomas R, Stein HJ, Rhede D (2007) Dating multiply overprinted Sn-mineralized granites—examples from the Erzgebirge, Germany. *Mineral Deposita* 42:337–359. <https://doi.org/10.1007/s00126-006-0114-2>
- Scaillet S, Cheilletz A, Cuney M, Farrar E, Archibald DA (1996) Cooling pattern and mineralization history of the Saint Sylvestre and western Marche leucogranite pluton, French Massif Central: I. <sup>40</sup>Ar/<sup>39</sup>Ar isotopic constraints. *Geochim Cosmochim Acta* 60:4653–4671. [https://doi.org/10.1016/S0016-7037\(96\)00291-8](https://doi.org/10.1016/S0016-7037(96)00291-8)
- Sibson RH (1990) Conditions for fault-valve behaviour. *Geol Soc Lond Spec Publ* 54:15–28. <https://doi.org/10.1144/GSL.SP.1990.054.01.02>
- Sibson RH (1987) Earthquake rupturing as a mineralizing agent in hydrothermal systems. *Geology* 15:701–704. [https://doi.org/10.1130/0091-7613\(1987\)15<701:ERAAMA>2.0.CO;2](https://doi.org/10.1130/0091-7613(1987)15<701:ERAAMA>2.0.CO;2)
- Stacey JS, Kramers JD (1975) Approximation of terrestrial lead isotope evolution by a two-stage model. *Earth Planet Sci Lett* 26:207–221. [https://doi.org/10.1016/0012-821X\(75\)90088-6](https://doi.org/10.1016/0012-821X(75)90088-6)
- Strong DF, Hanmer SK (1981) The leucogranites of southern Brittany; origin by faulting, frictional heating, fluid flux and fractional melting. *Can Mineral* 19:163–176
- Tartèse R, Boulvais P (2010) Differentiation of peraluminous leucogranites “en route” to the surface. *Lithos* 114:353–368. <https://doi.org/10.1016/j.lithos.2009.09.011>
- Tartèse R, Boulvais P, Poujol M, Gloaguen E, Cuney M (2013) Uranium mobilization from the Variscan Questembert syntectonic granite during fluid-rock interaction at depth. *Econ Geol* 108:379–386. <https://doi.org/10.2113/econgeo.108.2.379>
- Tartèse R, Boulvais P, Poujol M, Chevalier T, Paquette JL, Ireland TR, Deloule E (2012) Mylonites of the South Armorican Shear Zone: insights for crustal-scale fluid flow and water-rock interaction processes. *J Geodyn* 56–57:86–107. <https://doi.org/10.1016/j.jog.2011.05.003>

- Tartèse R, Ruffet G, Poujol M, Boulvais P, Ireland TR (2011b) Simultaneous resetting of the muscovite K-Ar and monazite U-Pb geochronometers: a story of fluids. *Terra Nova* 23:390–398. <https://doi.org/10.1111/j.1365-3121.2011.01024.x>
- Tartèse R, Poujol M, Ruffet G, Boulvais P, Yamato P, Košler J (2011a) New U-Pb zircon and  $^{40}\text{Ar}/^{39}\text{Ar}$  muscovite age constraints on the emplacement of the Lizio syn-tectonic granite (Armorican Massif, France). *Comptes Rendus Geosci* 343:443–453. <https://doi.org/10.1016/j.crte.2011.07.005>
- Tischendorf G, Förster HJ (1994) Hercynian granite magmatism and related metallogenesis in the Erzgebirge: a status report. Mineral deposits of the Erzgebirge/Krusné hory (Germany/Czech Republic). *Monogr Ser Mineral Deposits* 31:5–23
- Turpin L, Leroy JL, Sheppard SMF (1990) Isotopic systematics (O, H, C, Sr, Nd) of superimposed barren and U-bearing hydrothermal systems in a Hercynian granite, Massif Central, France. *Chem Geol* 88: 85–98. [https://doi.org/10.1016/0009-2541\(90\)90105-G](https://doi.org/10.1016/0009-2541(90)90105-G)
- Turrillot P, Augier R, Faure M (2009) The top-to-the-southeast Sarzeau shear zone and its place in the late-orogenic extensional tectonics of southern Armorica. *Bull Soc Geol Fr* 180:247–261. <https://doi.org/10.2113/gssgfbull.180.3.247>
- Vignerresse JL (1999) Intrusion level of granitic massifs along the Hercynian belt: balancing the eroded crust. *Tectonophysics* 307: 277–295. [https://doi.org/10.1016/S0040-1951\(99\)00104-3](https://doi.org/10.1016/S0040-1951(99)00104-3)
- Vignerresse JL, Brun JP (1983) Les leucogranites armoricains marqueurs de la déformation régionale; apport de la gravimétrie. *Bull Soc Geol Fr* S7–XXV:357–366. <https://doi.org/10.2113/gssgfbull.S7-XXV.3.357>
- Vignerresse JL, Cuney M, Jolivet J, Bienfait G (1989) Selective heat-producing element enrichment in a crustal segment of the mid-European Variscan chain. *Tectonophysics* 159:47–60. [https://doi.org/10.1016/0040-1951\(89\)90169-8](https://doi.org/10.1016/0040-1951(89)90169-8)
- Whitney DL, Evans BW (2010) Abbreviations for names of rock-forming minerals. *Am Mineral* 95:185–187. <https://doi.org/10.2138/am.2010.3371>